The Ganymede Laser Altimeter (GALA) on the Jupiter Icy moons Explorer (JUICE) Mission

Hussmann, Hauke; Lingenauber, Kay; Stark, Alexander; Enya, Keigo; Thomas, Nicolas; Lara, Luisa M.; Althaus, Christian; Araki, Hiroshi; Vermeersen, Bert; More Authors

DOI
10.1007/s11214-025-01149-7

Publication date
2025

Document Version
Final published version

Published in
Space Science Reviews

Space Science Reviews (2025) 221:33
https://doi.org/10.1007/s11214-025-01149-7

The Ganymede Laser Altimeter (GALA) on the Jupiter Icy moons Explorer (JUICE) Mission

Hauke Hussmann · Kay Lingenauber · Alexander Stark · Keigo Enya · Nicolas Thomas · Luisa M. Lara et al. ***[full author details at the end of the article]***

Received: 7 June 2024 / Accepted: 12 February 2025 / Published online: 18 March 2025

Abstract

The *Ganymede Laser Altimeter* (GALA) on the *Jupiter Icy Moons Explorer* (JUICE) mission, is in charge of a comprehensive geodetic mapping of Europa, Ganymede, and Callisto on the basis of Laser range measurements. While multiple topographic profiles will be obtained for Europa and Callisto during flybys, GALA will provide a high-resolution global shape model of Ganymede while in orbit around this moon based on at least 600 million range measurements from altitudes of 500 km and 200 km above the surface. By measuring the diurnal tidal deformation of Ganymede, which crucially depends on the decoupling of the outer ice shell from the deeper interior by a liquid water ocean, GALA will obtain evidence for (or against) a subsurface ocean on Ganymede and will provide constraints on the ice shell thickness above the ocean. In combination with other instruments, it will characterize the morphology of surface units on Ganymede, Europa, and Callisto providing not only topography but also measurements of surface roughness on the scale of the laser footprint, i.e. at a scale of about 50 m from 500 km altitude, and albedo values at the laser wavelength of 1064 nm. GALA is a single-beam laser altimeter, operating at a nominal frequency of 30 Hz, with a capability of reaching up to 48 Hz. It uses a Nd:YAG laser to generate pulses with pulse lengths of 5.5 ± 2.5 ns. The return pulse is detected by an Avalanche Photo Diode (APD) with 100 MHz bandwidth and the signal is digitized at a sampling rate of 200 MHz providing range measurements with a sub-sample resolution of 0.1 m. Research institutes and industrial partners from Germany, Japan, Switzerland and Spain collaborated to build the instrument. JUICE, conducted under responsibility of the European Space Agency (ESA), was successfully launched in April 2023 and is scheduled for arrival at the Jupiter system in July 2031. The nominal science mission including multiple close flybys at Europa, Ganymede, and Callisto, as well as the final Ganymede orbit phase will last from 2031 to 2035. In May 2023 GALA has completed its Near-Earth Commissioning, showing full functionality of all units. Here we summarize the scientific objectives, instrument design and implementation, performance, and operational aspects of GALA.

This paper is dedicated to the GALA system engineer Dr. Reinald Kallenbach, who passed away on March 5, 2023

1 Introduction

The *Ganymede Laser Altimeter* (GALA)[1] is one of ten payload instruments on ESA's *Jupiter Icy Moons Explorer* (JUICE) mission (Grasset et al. 2013; Witasse et al. 2025, this collection) which was successfully launched on an *Ariane* 5 rocket on April 14, 2023 from the *Centre Spatial Guyanais* in Kourou, French Guyana. GALA's main purpose is to provide topographic measurements of the icy moons of Jupiter —Ganymede, Europa, and Callisto— by measuring the distance from the spacecraft to the surfaces of these satellites. A second major goal is the detection of Ganymede's putative global subsurface water ocean and further characterization of the hydrosphere by monitoring the dynamic response of the ice shell to tidal forces exerted by Jupiter along Ganymede's eccentric orbit. Furthermore, GALA will contribute to the geological characterization of surface features on the icy satellites by providing accurate topography on global, regional, and local scales. It will also provide surface roughness and albedo measurements at the laser wavelength of 1064 nm on various spatial scales down to a few tens of meters, the size of the GALA footprint on the surface at a spacecraft altitude of a few hundred km.

With a radius of 2631.2 ± 1.7 km (Archinal et al. 2018) Ganymede is the largest satellite in the solar system. Gravity field data acquired by the *Galileo* spacecraft —and more recently *Juno*— together with spectral data of the surface suggest that Ganymede's interior is composed of water ice and rock-metal components in a mass ratio of about 40% (H_2O) to 60% (rock + metal). Ganymede is strongly differentiated (Schubert et al. 2004; Gomez Casajus et al. 2022; Hussmann et al. 2023). Most remarkably, Ganymede has an intrinsic magnetic field which is most likely maintained by dynamo action in a liquid Fe-FeS core (Kivelson et al. 1996; Schubert et al. 1996). Models that satisfy Ganymede's mean density and moment-of-inertia constraints of 1942.0 ± 4.8 kg m^{-3} and 0.3115 ± 0.0028, respectively, suggest Ganymede's interior to be composed of an iron-rich core surrounded by a silicate rock mantle and overlain by an ice shell (Anderson et al. 1996; Sohl et al. 2002; Schubert et al. 2004). The latter is expected to contain a briny subsurface water ocean located between a high-pressure water ice layer and the outermost ice shell (Spohn and Schubert 2003). The tidal response of Ganymede is indicative to the presence and extension of a subsurface ocean (Moore and Schubert 2003). Therefore, GALA is designed to measure not only the topography of Ganymede but also its large-scale tidal surface deformations. Measurements of the tidal potential from Doppler-tracking (3GM) along with the induced magnetic response of the ocean to the external Jovian magnetosphere(J-MAG) and Plasma Wave Instrument (RPWI) will additionally constrain the ocean properties. In particular, the depth at which the ocean in located with its electrical conductivity, and thus salinity.

GALA will obtain accurate height profiles along-track, i.e. in flight direction along the orbit velocity vector, for geomorphological interpretation of surface features. Impact basins, tectonic structures, which are present across large fractions of Ganymede's surface, as well as potential cryovolcanic features will be analyzed with GALA ground-tracks. Context information, especially from camera (JANUS), subsurface radar (RIME) and spectroscopic data (MAJIS) will be essential to understand the processes that have shaped Ganymede's terrain over its geologic history.

GALA will, mainly in combination with camera and radio science data, also contribute to the exact determination of the rotation state of Ganymede and, to lesser extent, also constrain the rotational states of Europa and Callisto. Combined with shape data of the satellites,

[1] As well see list of abbreviations in this article. We refer the reader also to the JUICE acronyms list at https://www.cosmos.esa.int/web/juice/juice-acronyms.

this will lead to a refinement of reference systems of the satellites. With GALA being the first laser altimeter ever flown to an icy satellite, the geodetic characterization of Europa, Ganymede and Callisto will significantly be improved. Again a combination with other instruments, mainly with radio science (3GM) and imaging data (JANUS) will be crucial to acquire optimum geodetic data-products and precise reference systems.

1.1 The JUICE Mission

In 2012, the JUICE mission (Grasset et al. 2013) was selected as the first L-class mission in ESA's *Cosmic Vision* program. It was successfully launched in 2023 and will reach the Jovian system in 2031 after almost 8 years of cruise. The Jovian tour includes two Europa flybys as well as multiple Callisto and Ganymede flybys before entering orbit around Ganymede in 2034. Details on the spacecraft and trajectory can be found in Boutonnet et al. (2024, this collection). For GALA the most important phases of the mission are the close —i.e., less than 3200 km altitude above the surface— flybys of Europa, Ganymede and Callisto, the pericenter passages of the elliptical orbital phase around Ganymede, and the final low-altitude orbits around Ganymede at altitudes of 500 km and 200 km, respectively.

2 Scientific Investigations of GALA

GALA will address scientific questions for the three satellites Ganymede, Europa, and Callisto. In the following we will discuss Ganymede —the main focus of the JUICE mission— first and then summarize the scientific questions addressed for Europa and Callisto at flybys during the Jupiter tour.

2.1 Ganymede

In general, GALA objectives for Ganymede will contribute to surface science —topography, surface roughness and reflectivity— (Tosi et al. 2024, this journal), to the interior of the moon —topography combined with gravity field data, tides, rotational state— (Van Hoolst et al. 2024, this collection), and to the geodetic definition of reference systems.

2.1.1 Topography and Shape

Topography and shape, a major focus of the GALA instrument, is related to scales of several thousands of km (global), to hundreds of km (regional) and down to a few tens of km or less (local). On all these scales topographic information is key to understand the satellite's evolution and the processes that have shaped its surface on regional and local scales.

i) Global Shape

Like all major satellites in the solar system, Ganymede is locked in a 1:1 spin-orbit coupling with respect to its central planet, in this case Jupiter, i.e. its orbital period of 7.15 days is synchronized with its spin period. On long time-scales a synchronously rotating satellite will assume an equilibrium shape with —apart from libration effects— its long axis a pointing towards the central planet, the polar axis c being the shortest axis due to rotational oblateness, and with the in-orbit axis b ranging in-between. From equilibrium theory (Hubbard and Anderson 1978; Dermott 1979; Zharkov et al. 1985) the expected shape can be predicted for both homogeneous and differentiated satellites. However, whether the satellite has actually assumed equilibrium depends on its thermal state which has a strong influence on material parameters, such as rigidity and viscosity. These parameters are frequency-

dependent and would tend to evolve towards equilibrium on long time-scales, i.e. on an infinite period. From several *Galileo* flybys, the fluid tidal potential Love-number of second degree and order $k_f = 0.804 \pm 0.018$ was determined for Ganymede (Schubert et al. (2004) and references therein), corresponding to a fluid radial displacement Love number of $h_f = 1 + k_f = 1.804 \pm 0.018$ in hydrostatic state. These values are consistent with a highly differentiated satellite, and the corresponding axes can be computed (e.g., Zharkov et al. 1985) as $a = 2633.40$ km, $b = 2632.04$ km, and $c = 2631.59$ km. The maximum difference of $a - c = 1.8$ km is on the order of a few km, which could be detected from imaging and laser altimetry data in orbit. Zubarev et al. (2015) have determined Ganymede's shape from a control-point network using *Galileo* imaging data and find that the derived tri-axial shape is consistent with equilibrium theory and earlier determinations by Davies et al. (1998). However, more accurate data would be needed to identify additional topographic variations and an exact orientation of the ellipsoid with respect to Jupiter and its time-variability due to librations. GALA measurements will thus provide accurate data for determining Ganymede's tri-axial shape in the course of the JUICE mission. A reference ellipsoid will be derived from shape data to which regional and local altimetry measurements can be referred.

Combined low-order gravity and altimetry measurements will reveal whether Ganymede is in hydrostatic equilibrium taking into account rotational and tidal forces. Deviations from the expected geoid will tell us whether the interior can sustain long-wavelength topography over long timescales. Interpretation of such a long-wavelength topography could include i) a very rigid outer ice shell that did not yet adjust to an equilibrium state; ii) latitudinal and/or longitudinal variations of ice thickness according to the thermal state of the ice shell and ocean; iii) gravitational influence of the silicate interior on the outer ice shell (e.g., Pauer et al. (2010) in application to Europa). Furthermore, global shape data will be used to determine center-of-figure/center-of-mass offsets. Again the combination with gravity field data is essential here.

ii) Low-Degree Topography

Whether lateral variations of topography on the order of thousand km are present on Ganymede is unknown. Such topography anomalies superimposed on the degree-2 topography could be caused by density variations in the interior. Correlation between gravity and topography would indicate deviations from isostatic compensation with important implications for the thermal state of the lithosphere. Therefore, combined gravity and topography measurements are key to understanding the thermal evolution of the outer ice shell. Inhomogeneous mass distributions in the ice can be caused by convection, impact remnants buried in the ice, or by large scale topography at the rock/ice interface. Gravity anomalies at scales of a few thousand km on Ganymede have been reported by Palguta et al. (2006, 2009). Combined gravity and topography data at the given locations could reveal whether the mass anomalies are located deep inside the interior (possibly associated with the rock/ice boundary) or correlated with surface topography and geological terrain. Multi-ring impact basins, e.g. the large basin *Gilgamesh*, have similar dimensions. The gravity corrected for topography would reveal whether such basins show anomalies associated with mass concentrations related to the impact.

iii) High-Degree and Regional Topography

Topography provides a specific record of the evolution processes and lithospheric structure of a planetary body. It can be used to infer lithospheric thickness and, using yield-strength envelopes (Golombek and Banerdt 1986; Giese et al. 2008), thereby determining the body's thermal state at the time of (topography) formation. Laser altimeter profiles are an effective method for deriving topography. However, to infer the thickness of the lithosphere there is a need for additional information. First of all, the location of the profiles in

relation to the covered feature is required, and the process that has formed the feature must be known. Ideally this context information is provided by imaging data appropriate to infer the effective elastic thickness of the lithosphere (Nimmo et al. 2002). In order to get such topography information from altimetry profiles the lateral spacing between the profiles must not be larger than a few km. A promising method to obtain a lower bound on lithospheric thickness is to relate the bending moment computed from topography to the overall strength of the lithosphere computed from a Yield-Strength Envelope (Luttrell and Sandwell 2006). This requires geologic context information on the profiled features. Thus, local topography will help to understand the formation of geological features that are related to the structure of the outer icy crust, the processes involved in its deformation and the specific fate of water in this layer adjacent to the conjectured internal ocean. On Ganymede, the high strain tectonism suggested by the observed grooved terrain (e.g. Pappalardo et al. 1998) and possibly cryovolcanism both give indications on the rheology and thermal state of the icy crust.

Depending on temperature, the ice shell on Ganymede might be in a convective state. In that case convection in the outer crust would be restricted to a layer thinner than 200 km either due to the presence of an internal ocean or due to a phase change in the ice from ice-I to ice-III (Bland et al. 2009). The corresponding wavelength of the resulting topography at the surface due to upwelling plumes (or downwellings) will probably be too small to be referenced to the Ganymede geoid. However, regional features referenced to the global shape of Ganymede would be indicative of dynamic processes within the ice shell (e.g., Golle et al. 2012).

Convection is driven by temperature differences of several tens of K, resulting in approximate density variations of 0.1 to 0.2 kg m^{-3}. In the lower high-pressure ice shell, which is approx. 600 km thick, a column of cold (or warm) ice 100 km in radius would produce a gravity anomaly —if uncompensated by variations in density and topography— at 100 km altitude of approx. 0.03 mgal. In the upper shell, which is approx. 150 km thick, a column of cold material 30 km in radius would produce an uncompensated anomaly of approx. 0.01 mgal. The compensating topography at the surface for the upper layer example above is approximately 20 m (over approx. 60 km). Therefore, GALA will search for topography at 30 to 300 km wavelengths in the upper ice shell. With respect to the Ganymede geoid, only longer wavelength features of the convection pattern within the ice shell can be retrieved: these could be caused by lateral variations in the composition of ice leading to variations of thermodynamical parameters (such as density, thermal expansion or thermal conductivity) or to radiogenic production of heat. For Ganymede and Callisto, it is very unlikely that heterogeneous tidal heating of the icy crust at present will lead to such a long wavelength structure of the convective pattern — contrary to what is predicted for Europa (Tobie et al. 2003) or Enceladus (Behounkova et al. 2012). They may have been important though in Ganymede's past due to a possibly higher orbital eccentricity during resonance passages (Showman and Malhotra 1997). Thus, both long-wavelength and short wavelength topography will be analysed to study Ganymede's thermal history. By combining data from laser altimetry with camera (Palumbo et al. 2025, this collection), subsurface radar (Bruzzone et al., this journal), and spectroscopic data (Poulet et al., this journal) the JUICE instrumentation is perfectly suited to investigate processes that have shaped the surface and shallow-subsurface (km to tens of km range) of the icy moons.

2.1.2 Tides

The detection of Ganymede's global subsurface water ocean and further characterization of the water-ice/liquid shell require monitoring of the dynamic response of the ice shell to tidal forces exerted by Jupiter along Ganymede's eccentric orbit. The second-degree body tide

Love numbers k_2 and h_2 are measures for the variation of the gravitational potential due to tidally induced internal redistribution of mass and the corresponding radial surface displacement relative to the height of the tidally unperturbed geoid, respectively. These body-tide Love numbers depend on the internal structure and rheology of a planetary body, in particular, on the presence of internal fluid layers and the thickness and shear strength of an overlying solid shell. h_2 and k_2 are affected in similar, but not in identical ways, by the details of the mechanical structure of the interior. Whereas k_2 can be inferred from time-variable contributions to the low-degree coefficients $J_2 = -C_{20}$ and C_{22} of the gravitational field (Iess et al. 2025, this collection), h_2 can be measured by laser altimetry determining global shape variations from range measurements at cross-over points obtained at different tidal phases of the moons revolving about Jupiter (Steinbrügge et al. 2015). For this purpose, precise orbit determination as well as accurate pointing knowledge of the transmitter bore-sight is required. In its final mission phase, the JUICE spacecraft will enter a 500-km circular orbit (above surface) around Ganymede and a 200-km circular orbit in the mission's extended phase. In these phases Ganymede's tidal Love number h_2 will be determined which would (a) confirm whether a subsurface ocean is present below Ganymede's outer ice-I shell and (b) provide constraints on the thickness of the outer ice-I shell. Surface deformations would be an order of magnitude larger in the presence of a subsurface ocean, as compared to a completely solid interior. For a given interior structure and rheology model the Love numbers are depending almost linearly on ice thickness (Moore and Schubert 2000, 2003). The dependencies on rheologic parameters, in particular rigidity and viscosity has been investigated by Kamata et al. (2016).

The knowledge of both body tide Love numbers, h_2 and k_2, and the simultaneous determination of linear combinations of the latter reduce the ambiguity in structural models and the dependence of the measurement on material parameters, e.g. the ice rigidity (Wahr et al. 2006; Hussmann et al. 2011; Kamata et al. 2016; Kimura et al. 2019). A joint analysis of altimetry and radio science data from 3GM (Iess et al. 2025; Van Hoolst et al. 2024, both this collection), would be an optimum strategy to determine the ice shell thickness. This data will best constrain the ice shell and ocean thickness in combination with measured induced magnetic fields (Dougherty et al. 2025, this collection).

2.1.3 Surface Morphology

On a global scale, Ganymede's surface can be divided into two terrain types: about one third of the surface is covered by heavily cratered dark terrain typically modified by the presence of large-scale arcuate fracture systems termed *furrows* (Pappalardo et al. 2004; Prockter et al. 2010). The formation of furrows may be related to ancient impact events on a global scale (e.g., Hirata et al. (2020)). The remaining two thirds are bright regions, also called *grooved terrain*. Smaller crater densities indicate a younger age of the latter regions as compared to dark terrain. Surface morphology suggests that they were formed by intense tectonism that produced a complex system of extensional linear structures of horst and graben relief (e.g. Pappalardo et al. (1998), Giese et al. (1998), Prockter et al. (1998), Head et al. (2002)), but relatively smooth areas are also present. Cryovolcanism has been considered as possible formation mechanism for the latter (Prockter et al. 2010), but available data have not provided sufficient resolution and coverage for further enforcing this hypothesis.

Detailed topographic profiles crossing the linear features of grooved terrain as well as digital elevation models (DEMs), produced from the dense altimetry coverage obtained from the circular orbit phase, will be central for characterizing the tectonic styles and processes

associated with groove formation, as well as for mapping regional tectonic systems that form natural boundaries for the analysis of large-scale crustal deformation. For example, topographic profiles acquired by GALA normal to the strike of structural landforms such as normal faults are ideal to quantify strain. When coupled with chronological information from images (crater size-frequency distributions), it might even be feasible to derive strain rates. Ideally, such investigations benefit also from context information from high-resolution images of the camera experiment, as well as from stereo image-derived DEMs. Specific targets on Ganymede for Juice that are also relevant for the coverage with GALA ground-tracks have been identified by Stephan et al. (2021).

The topographic database derived from stereo imaging from the *Galileo* and *Voyager* datasets is very limited. The available data suggest that Ganymede's surface has limited topographic variation of typically less than a km as observed also for Europa. Generally, old dark terrain features seem to have stronger relief than younger, bright terrain features. The features with largest relief are domes showing relief of up to 2.5 km (Prockter et al. 2010). The images of Ganymede returned by *Galileo* provide only limited coverage of the surface. Only a small subset of the dataset could be used to derive topography from stereo imaging (e.g., Giese et al. (1998)). High-resolution images and high-resolution stereo models (meter-scale resolution up to tens of meters) will most likely be available only for a small fraction of the surface.

Whereas the requirements from gravity and geophysics are stringent with respect to height resolution but generous in terms of spatial resolution, for geology, dense spatial coverage, high spatial resolution and high resolution of topographic heights are all important because of the smaller scale of the tectonic and possibly cryo-volcanic features. Combined with global image coverage (assuming 100-400 m/pixel), GALA operating at 30 to 48 Hz combined with a laser footprint of 20 to 50 m diameter, respectively, will provide excellent along-track coverage. For the given near-polar orbit the gaps in longitude between the tracks will be largest in equatorial regions. These gaps can exceed 20 km in extreme cases. However, specific gaps can be filled by off-nadir pointing of the spacecraft. Accurate co-registration of the camera data with the altimetry data will benefit from methods applied for data of recent planetary missions.

2.1.4 Surface Roughness

Slopes and roughness are important parameters for quantitative studies of surface characteristics. Surface roughness of icy bodies at different spatial scales —from meters to several km— is a result of competing processes that modify their surfaces, including impact cratering, tectonics, (cryo)volcanic resurfacing, sublimation, and space weathering (e.g., Aharonson et al. (2001) for Mars; Cheng et al. (2001, 2002) for asteroid 433 Eros; Rosenburg et al. (2011) for the Moon). To date the dominant factors affecting these parameters are known to vary with baseline scale and geologic environment especially. GALA will have the capability to assess the surface roughness by analyzing digitized return signals. With the latter, a better separation of surface roughness (on meters-scale) and local slope effects can be expected. An important objective is to relate the surface roughness to different terrain types on Ganymede. Similarly, surface roughness may also be an indicator of terrain age, as surfaces of the same type might, e.g., get smoother with time due to sublimation effects. To characterize surface roughness at Ganymede, laser footprints of about 50 m in diameter and high shot frequencies will be used in the Ganymede orbit phases. Analysis of the digitized sample of the return pulse by GALA provides essential data sets for surface roughness. Thereby the GALA return pulse spreading will be used to determine the surface roughness on the

scale of the laser footprint of 50 m. From consecutive spots the surface slopes and different scales will be obtained (e.g., Kimura et al. (2019)). Measurements of surface roughness on the footprint scale can be correct from slopes using such a data set. JUICE will provide the first measurements of surface roughness down to the tens of meters scale for an icy satellite (as opposed to the terrestrial planets where corresponding data sets are available for Mars, Mercury and the Moon). Furthermore, surface roughness measurements will be used to characterize possible landing sites for future landed elements.

2.1.5 Albedo

A laser altimeter can obtain key data on surface albedo at the corresponding laser wavelength, in this case 1064 nm. The icy satellites all show high reflectivities in the 1-micron range (Madden and Kaltenegger 2018). As the altimeter carries its own light source, the albedo measurements do not depend on corrections of photometric (illumination) effects. Hence, better controlled measurements of albedo —though restricted to the narrow bandwidth of the laser— are possible. Laser altimeter observations become particularly important in areas of permanent shadow, where camera observations are not at all possible. Such measurements would complement the data sets from the spectrometer. Correlation of albedo with geological units and the relation to Ganymede's magnetic field and interaction with the Jovian magnetosphere will be studied in detail. Analysis of stereo topographic models obtained from *Galileo* images has revealed a strong correlation between elevations and material (Giese et al. 1998; Oberst et al. 1999). In some areas, bright material appears to be concentrated on slopes tilted north within *Galileo Regio*. Possibly, thermal migration of ice in combination with mass wasting can explain these patterns (Spencer 1987; Stephan et al. 2020). GALA will map such albedo patterns and study their relationships to topographic elevations and slopes.

2.2 Europa and Callisto

In addition to the investigation of Ganymede with JUICE in orbit around the satellite and during flybys in the Jupiter orbit phase, the spacecraft will perform two flybys at Europa and various flybys at Callisto. GALA will be able to acquire data from the two Europa flybys with a closest approach of 400 km altitude, and from the closest 15 Callisto flybys below 1100 km. The following investigations of Europa and Callisto will be carried out by GALA.

2.2.1 Europa

The present JUICE trajectory includes two Europa flybys, without the opportunity for crossing altimetry profiles on Europa's surface at different tidal phase in orbit around Jupiter. It is therefore impossible to measure Europa's tidal distortion in this scenario. Hence, potential GALA measurements (two laser tracks as shown in Fig. 23) will focus on retrieving the global shape of Europa and at the same time on acquiring data for the geomorphological characterization of surface features and on supporting the interpretation of the subsurface radar signals.

Europa's diverse geology is unique in the solar system. Spreading-style crustal deformation is known to be a dominant process of surface formation (Greeley et al. 2004), while chaos regions and ridges are most certainly associated with melting (e.g. Schmidt et al. (2011), Culberg et al. (2022)) and melt migration within the icy crust (Steinbrügge et al. 2020). GALA's high frequency mode with laser shots at 48 Hz is appropriate to obtain height

profiles with a spot distance of about 20 m when the spacecraft is closer to the surface than about 1300 km. Along the two tracks several regions are located that are associated with recent activity or possible cryovolcanism, presumably involving liquid water as indicated by smooth plains. *Conamara Chaos* is an example of chaotic terrain for which topography was derived from *Galileo* stereo imaging data. Although this region is not located along the two tracks planned for JUICE it shows the typical features of chaos terrain. Ice blocks are broken apart, tilted, and shifted within the matrix material which appears to be at different topographic levels. GALA's objective during the flybys is to derive slopes and the topographic levels of different geologic units along the altimeter track with high vertical resolution (orders of meters), with little distance between the laser footprints. Analysis of the return pulse would allow for the determination of surface roughness on the scale within the spot-size.

A fundamental question related to the formation of chaos terrain is whether chaotic regions are elevated regions with respect to the surrounding reference surface. Positive topography with respect to the surrounding terrain would suggest upwelling plumes as the fundamental formation process (Pappalardo et al. 1999). An alternative scenario favors regional liquid water reservoirs associated in the shallow subsurface (Schmidt et al. (2011)). Such water reservoirs would be associated with topographic lows due to the higher density of liquid water as compared to solid ice. The expected long-scale topographic variations to be measured by GALA would be on a lateral order of tens to hundreds of km. Digital terrain models based on laser altimetry optionally combined with stereo-imaging data would be the optimum method to distinguish between these different formation scenarios.

Besides chaotic regions double ridges, bands, smooth plains, pits, spots and domes, and craters would be sites of specific interest along the tracks. Again the synergy between laser altimetry, camera, spectrometers and subsurface radar for these targeted observations would provide most valuable data sets to infer the dynamics and recent (or ongoing) activity in Europa's ice shell.

2.2.2 Callisto

Whereas Ganymede and Europa show regions that have been modified extensively by endogenic geological processes, the surface of Callisto is dominated by craters of various sizes (Moore et al. 2004). Laser altimeters are ideal tools to characterize crater morphologies, as ideally a single topographic profile through the crater center is sufficient, assuming an axisymmetric shape. Besides impacts, surface modifications on Callisto are almost entirely based on weathering processes and erosion. Whereas height profiles obtained during flybys would reveal crater morphologies of various types, surface roughness measurements are the tool to characterize different degrees of surface degradation. GALA will address both objectives during the Callisto flybys (see Fig. 23). The former would be related to impact formation and different rheological structure and temperature profiles of the shallow ice at time of formation. Specific targets during the flybys at Callisto would include the wealth of different impact structures, as also observed on Ganymede (Schenk et al. 2004), including *simple craters*, craters with *central pits* and *domes* with diameters of several tens of km, *Palimpsests* and *multi-ring structures* with diameters of several hundreds to a few thousand km. Of special interest are crater chains as a result of tidally disrupted impactors, fresh impact craters at which bright ice at the impact site and in the ejecta was recently exposed to open space, as well as relaxed craters indicating higher temperatures and viscous relaxation within the shallow ice shell after the impact.

Palimpsests are unique impact structures on Ganymede and Callisto that are devoid of typical crater morphologies such as crater rims (Jones et al. 2003; Pappalardo et al. 2004).

Hypotheses for the origin of such heavily eroded and relaxed impact structures include the following modes of emplacement: (a) extrusion, triggered by impact, (b) fluidized ejecta, (c) dry and solid ejecta. To distinguish between those by profiling the surface and subsurface is a fundamental task of laser altimetry, imaging systems, and subsurface radar.

Geodetic observations obtained from global and regional laser tracks would be used to determine the global shape of Callisto. This would have important implications on Callisto's hydrostatic state or for deviations from the latter. Whether tidal distortion and/or the physical librations of Callisto can be determined is questionable given the limited number of flybys. Similar to Europa the GALA measurements at Callisto will focus on geomorphologic characterization of surface features by obtaining local and regional height profiles.

2.3 Reference Frames and Cartography

The accurate determination of rotational parameters by GALA will enable us to re-define the reference frame for Ganymede. Steinbrügge et al. (2019) have studied the possibility to derive the rotational state of Ganymede's outer ice shell by using topography measured by laser altimetry based on either a spherical harmonics expansion or B-splines on a rectangular grid. According to these studies, GALA can measure the amplitude of Ganymede's librations with an accuracy of 2.5 to 6.6 μrad (6.6 to 17.4 m at the equator). This allows for determining the thickness of an elastic ice shell, if decoupled from the deeper interior by a subsurface ocean, to about an accuracy of 24 to 65 km. It will also lead to a refinement of the reference system including librations and possibly obliquity and precessions that are required for the production of accurate maps to which any measurement by JUICE and other missions could be referenced. In particular for high-resolution camera data, this will also be essential for targeting and navigation of potential future landers.

GALA will have excellent data coverage including large numbers of cross-overs (crossing laser ground-tracks) at the high-latitude regions of Ganymede. This will allow us to obtain reliable coordinate knowledge and to carefully study illumination conditions near the poles. The obliquity of Jupiter and the obliquity of Ganymede, as well as the orbital inclination of Ganymede are small. Hence, we expect polar areas on Ganymede at high latitudes, which are exposed to long daylight or Earth viewing geometry– information which is essential for future landers in terms of power and communications. Likewise, we may find craters in permanent darkness and unique thermal environments. Again, topography is essential here to identify the highs and lows near the poles, a task which GALA can fulfill very accurately and with excellent spatial coverage. It has to be noted though that the poles are not reached in nadir-pointed mode. The JUICE orbit is inclined and thus off-nadir pointing would have to be used to fill these gaps.

By providing accurate shape measurements at the flybys, GALA will also contribute to the geodetic characterization (shape and rotational state) of Europa and Callisto. The synergy of imaging data, combined with laser altimetry and gravity field data is essential to providing accurate geodetic reference systems.

2.4 Summary of GALA Science Objectives

The investigations to accomplish the overarching science goals of the JUICE mission (Witasse et al. 2025, this collection) to which GALA contributes are summarized here (Table 1). The measurement type indicates which information from the GALA return pulses are relevant for each objective. The range will be determined from the time-of-flight of the wave-package, the surface roughness from the width and shape of the return pulse, and the albedo from the intensity of the reflected pulse.

Table 1 Contributions of GALA to the JUICE Science Investigations

Investigation	GALA Measurement Type
Ganymede	
Determine the amplitude and phase of the gravitational tides	range
Characterize surface motion over Ganymede's tidal cycle	range
Determine the satellite's dynamical rotation state	range
Investigate the core and rocky mantle	range
Characterize the structure of the icy shell	range
Correlate surface features and subsurface structure	range, roughness, albedo
Determine the formation mechanism and characteristics of landforms	range, roughness, albedo
Relate compositions with their properties and distribution to geology	range, roughness, albedo
Europa	
Relate compositions with their properties and distribution to geology	range, roughness, albedo
Surface and sub-surface exploration for water reservoirs	range
Determine the minimal thickness of the icy crust in active regions	range
Search for possible active regions on the surface	range, roughness, albedo
Callisto	
Explore the structure and properties of icy crust and liquid shell	range, roughness, albedo
Relate compositions with their properties and distribution to geology	range, roughness, albedo
Determine the formation mechanism and characteristics of landforms	range, roughness, albedo
Investigate the interior of Callisto	range
Constrain global and regional surface ages	range, roughness, albedo

3 Measurement Technique and Instrument Overview

Laser Altimetry has widely been used in planetary applications, including the terrestrial planets (e.g., Sjogren and Wollenhaupt 1973; Zuber et al. 1994; Smith et al. 1999; Araki et al. 2009; Smith et al. 2010, 2017; Li et al. 2010) as well as small bodies (e.g., Zuber et al. 2000; Mukai et al. 2007; Seabrook et al. 2022). Various different data-products are derived from LiDAR measurements which are over mission duration typically based on several hundreds of millions individual laser shots at the target surface. For each laser shot we can acquire information on 1) the range from the spacecraft to the surface, 2) the roughness and slope of the terrain that is illuminated by the laser spot and 3) the albedo of the respective terrain at the laser wavelength. In the following we will discuss the technique for each of these measurements.

3.1 Range

The basic principle of a range measurement is the following: a short laser pulse with a typical pulse-width of a few ns is transmitted from the instrument on-board the spacecraft to the surface of the target body. The back-scattered laser pulse is received at the instrument's receiver telescope. From the measured time of flight Δt of the wave-package, the distance d to the surface can be computed by $d = c\Delta t/2$, where c is the speed of light in vacuum. The factor of 1/2 is required because the photons pass the distance d twice. Thus, 1 ns in Δt corresponds to approximately 15 cm in range. The typical time of flight for orbiter altitudes of a few hundred km is thus on the order of a few milliseconds. Despite this simple principle,

the technical challenges in realizing such a measurement are substantial. Not only the precision within the instrument (e.g., determination of accurate elapsed time between outgoing and received pulses) but also the position and orientation of the spacecraft at the time of the measurement have to be accurately known. Here we assume the general case including a small off-nadir pointing angle ϕ that has an uncertainty due to the limits in pointing knowledge. The measurement of the height h of the surface with respect to a reference surface R_{ref} (usually the geoid, but could also be a defined reference sphere) requires accurate knowledge on the spacecraft distance with respect to the center of mass $R_{s/c}$ and its orientation at the time when the measurement was taken. The height of the laser footprint can then be determined as

$$h = \sqrt{R_{s/c}^2 + d^2 - 2R_{s/c}d\cos\phi} - R_{\mathrm{ref}}. \tag{1}$$

With a number of at least 600 million individual range measurements, GALA will provide the topography and global shape of Ganymede with a vertical accuracy on the order of meters. In addition, these range measurements provide height profiles across geological units for their geo-morphological characterization, not only for Ganymede but also for the Europa and Callisto flybys.

3.2 Surface Roughness

In addition to the range, the shape of the return pulse of each individual laser shot contains information about the surface roughness and slope of the terrain. Both small-scale roughness and slope will broaden the return pulse due to the differing time-of-flight of the photons hitting rough or sloped terrain. Thus, the pulse broadening that is analyzed by the GALA electronics in the sampled return is a measure for slope and roughness. Taking into account the general trend of consecutive laser spots the pulse-broadening effect of the slope can be subtracted, if a specific baseline for the slope is chosen. The remaining effect on the pulse width can then be attributed to the small-scale roughness within the laser footprint of 50 m in diameter for the 500 km orbital altitude (see also Fig. 24).

3.3 Albedo

From the intensity of the transmitted and received pulse we can retrieve information about the reflectivity (albedo) at the laser wavelength of 1064 nm for each laser shot. The energy of the transmitted and reflected pulses can be determined from the sampling and fitting of the digitized pulse curves as the integrated area below the curve. Whereas the accuracy of the relative albedo will be on the order of a few percent, reference to absolute albedo values will be challenging to calibrate. Expected uncertainties for absolute values are on the order of about 20%. Thus it will be crucial to reference these values to complementary measurements from remote sensing instruments, in particular spectrometers and cameras from JUICE and previous missions.

3.4 The GALA Instrument

Here we give a brief overview on the instrument's main units and configuration. Details can be found in Sect. 5. GALA consists of three units (Fig. 1),

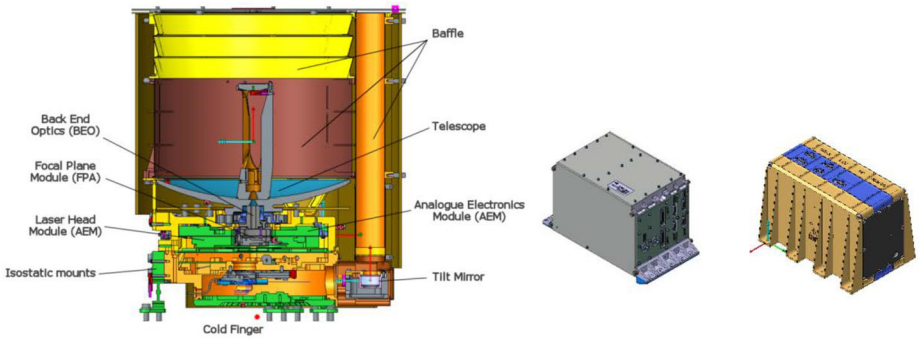

Fig. 1 GALA main units: Left: the transceiver unit (TRU) located on the optical bench of the spacecraft; middle and right the Electronics Unit (ELU) and Laser Electronics Unit (LEU), respectively, which are both located inside the spacecraft vault

1. the transceiver unit (TRU) includes the transmitter, receiver, the corresponding optics and baffles, the detector, and two redundant lasers including the pump diodes. The TRU is mounted on the optical bench of the spacecraft and is in operation pointed nadir to the moons' surfaces.
2. The Electronics Unit (ELU) is the electrical interface to the spacecraft. It includes the GALA software in the digital processing module (DPM, main + redundant), the power converter module (PCM, main + redundant) and the Range finder Module (RFM). With the DPM, the instrument is configured and operated via telecommands.
3. The Laser Electronics Unit (LEU) configures and triggers the laser. Both ELU and LEU are located within the vault of the spacecraft to shield the electronics from the harsh Jovian radiation environment.

The GALA hardware was developed and built within a consortium of institutes and industry from Germany, Japan, Switzerland and Spain. The responsibilities with respect to the units and sub-units are schematically shown in Fig. 2.

4 Environmental Constraints

Environmental conditions are a main driver for the instrument design on planetary missions. For JUICE, the two main environmental constraints that had to be considered in the instrument design originate from the mission specific thermal environment from launch, cruise and science phase and the radiation environment at Jupiter.

4.1 Thermal Environment

The laser altimeter has to cope with different thermal environments during the entire mission.

4.1.1 Launch

During launch, the instrument is switched off. The temperatures of the spacecraft and of the device increase as a consequence of the aerothermal load and of the exposition to the radiative heat fluxes (from the Sun and the Earth). This phase was the sizing case for the

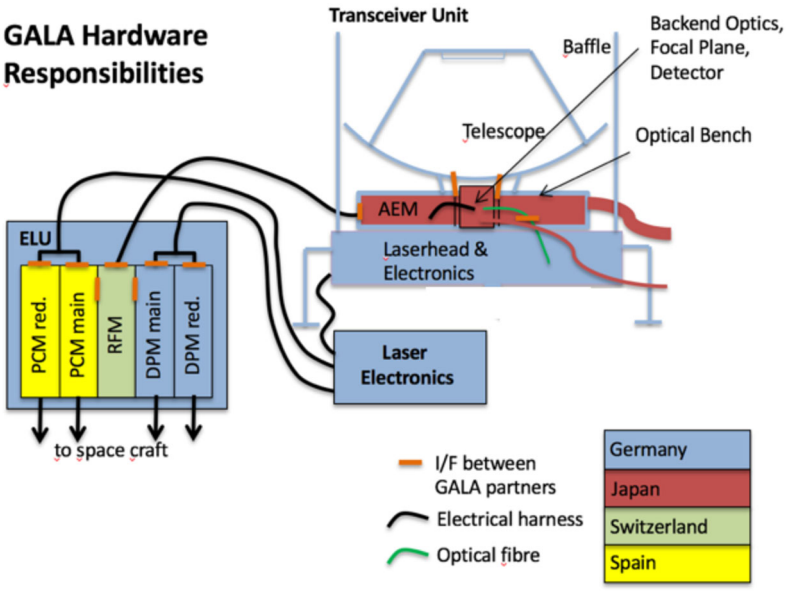

Fig. 2 GALA hardware units and responsibilities within the consortium. ELU: Electronics Unit; PCM: Power Converter Module; RFM: Range Finder Module; AEM: Analog Electronics Module; I/F: Interface; red.: redundant

external baffle for two reasons. First of all, because the baffle is directly exposed to the atmosphere, and thus to the aerothermal load. The second reason is that part of its surface is gold coated, significantly absorbing solar and albedo fluxes with a low re-emission in the infrared waveband. Even if unfavorable from a pure thermal point of view, the use of the gold coating is necessary for the optical performance of the baffle in the operational scenario at Ganymede. Fortunately, the aerothermal flux lasts 20 minutes only, reaching a peak as high as 1135 W/m^2.

4.1.2 Low Earth Orbit Phase (LEOP)

Immediately after launch, the instrument remains switched off. The satellite cannot guarantee attitude control: in the worst case, the Sun can directly impinge within the field of view of the instrument. Since the telescope and parts of the baffle are gold-coated, this possibility represents a potential danger in the same way as during the launch phase. Even more challenging, the sunlight collected by the primary mirror can be reflected and focused on the secondary mirror. In turn, the secondary mirror can reflect the concentrated optical power directly into the detector. If the sun illumination would be steadily maintained, the temperature of all these parts would rapidly increase beyond the limits of the coatings and of the materials. The sensitive detector would quickly be damaged with a prolonged sun illumination. For this reason, the spacecraft guarantees a minimum angular velocity rate of 0.5 deg/s and a maximum duration of Sun illumination of 20 min, including the LEOP before attitude control acquisition. In particular, the potentially high load on the detector has been limited to a very few seconds, preventing any possible damage.

4.1.3 Cruise Phase

For nearly its complete duration, the cruise is the coldest phase of the mission. GALA is switched off except for short tests and for calibration purposes. The trajectory includes flybys of Earth, Moon and Venus, bringing the spacecraft to a minimal distance to the Sun of 0.64 AU (Boutonnet et al. 2024, this collection). Even if it is planned to keep the sensitive instruments of JUICE in shade, a contingency scenario which involves attitude loss at the closest approach of the Sun must be considered in the design. For this worst-case scenario occurring during the Venus flyby phase, a maximum duration of 10 minutes sun illumination, during which the sun may impinge on GALA with an angle as low as 20° (half cone) with respect to the instrument line of sight was specified (more stringent than the 20 min mentioned above).

With nominal attitude, and in particular in the outer part of the solar system, the temperatures of the spacecraft and of the instrument will be low. Survival heaters have been implemented to prevent sensitive parts from reaching too low temperatures, which may cause damage due to thermo-elastic deformations or simply bringing electronics and electro-optical parts beyond their qualification range. The same heaters are also used to mitigate contamination effects. Outgassing and release of contaminants are expected to be high at the very beginning of cruise: the survival heaters are used to keep the contamination-sensitive surfaces hotter than other parts of the instrument (anti-contamination mode), favoring condensation and deposition of contaminants on colder, non-sensitive surfaces. In anti-contamination mode, the actual temperature is not relevant, only the temperature difference between contamination-sensitive (namely, the optics) and contamination-uncritical surfaces plays an important role. Anti-contamination mode can be achieved with a very low power consumption, and is planned to be maintained for the whole cruise phase. In order to clean the optical surfaces, forcing evaporation/sublimation of the already-deposited contaminants, the heaters will be operated in de-contamination mode: this entails maximum power dissipation, in compliance with the specified power density and temperature limits. The goal is to cause a rapid temperature increase up to the maximal achievable levels. The power consumption in de-contamination mode is high but for a short time; it is planned to perform de-contamination only in a few occasions during the mission, specifically at the beginning of cruise (when outgassing is high) and at the end (before start of nominal operations).

4.1.4 Ganymede Orbit Phase

The different orbits planned around Ganymede are, from a purely thermal point of view, similar to the last part of the cruise. The distance from the Sun is in the range from 4.95 to 5.45 AU and therefore the solar heat fluxes are negligible even in steady state sun pointing. The infrared emission from Ganymede is very low since the surface temperature is between 90 K and 160 K. The main difference from the cruise phase is the heat dissipated by the spacecraft and by the scientific instruments, which increase the temperature of the GALA boundaries. Even more important, in the 500-km orbit around Ganymede, the altimeter will be continuously operational for approximately 15.5 hours a day. The high electrical power consumption of the instrument (55.1 W in nominal Science mode) is almost completely converted into dissipated heat, which needs to be extracted from the instrument. Only the optical power of the laser, approximately 0.51 W, represents a power consumption which leaves the system without being converted into heat. The thermal control of the electronic boxes follows a standard approach, which consists of mounting the units on heat pipes managed by the spacecraft thermal control system. For the control of the optical head, a flexible

Table 2 Operational and non-operational temperature ranges of GALA

Unit	Position	non-ops. T_{min}	ops. T_{min}	perf. T_{min}	perf. T_{max}	ops. T_{max}	non-ops. T_{max}
ELU	TRP	−30 °C	−20 °C	−20 °C	+50 °C	+50 °C	+60 °C
ELU	radiative sink	−20 °C	−20 °C	−20 °C	+50 °C	+50 °C	+50 °C
LEU	TRP	−30 °C	−20 °C	−20 °C	+50 °C	+50 °C	+60 °C
LEU	radiative sink	−20 °C	−20 °C	−20 °C	+50 °C	+50 °C	+50 °C
TRU	cold finger I/F	−30 °C	+05 °C	+05 °C	+30 °C	+30 °C	+40 °C
TRU	mounting plate	−44 °C	−42 °C	−41 °C	−04 °C	−02 °C	+25 °C
TRU	radiative sink	−39 °C	−39 °C	−39 °C	+13 °C	+13 °C	+25 °C

thermal strap has been implemented on spacecraft side connected to the TRU main body to remove the waste heat. The thermal control of the optical head is of primary importance and it is made more difficult by the high power density of GALA (up to 23.9 W) to be extracted from the cold finger interface, which has a surface of only 30.5 cm^2. This critical interface is controlled by the spacecraft, maintaining the minimum temperature with heaters and limiting the maximum temperature by properly sizing the radiator. In order to minimize thermo-elastic deformations, the optical head is insulated by design from the mounting plate implementing bipods made of titanium and with bottlenecks in their cross-section. Finally, the unit is radiatively insulated from the spacecraft cavity and from the environment using gold coating on the external surfaces and wrapping the optical head with multi-layered insulation (MLI) blanket.

4.1.5 Boundary Temperatures

The following boundary temperatures (Table 2) are maintained by the spacecraft thermal control system at the GALA interfaces (the GALA units are described in Sect. 5):

4.2 Thermal Modelling

4.2.1 Objectives

Thermal models of the different GALA units have been developed starting from the very beginning of the design, with the goals to investigate the temperature levels in which the instrument will operate, the thermal gradients with associated thermal deformations and loss of optical performance, the impact of the environment on the instrument temperature and its stability, and the heat load forced onto the spacecraft thermal control system (TCS).

4.2.2 Software

For all these purposes, different thermal models with different levels of details have been developed. In particular, the reduced thermal models required by ESA to perform coupled analyses with the spacecraft had to be developed with the ESATAN-TMS suite. In order to ease model maintenance and correlation, the detailed models of LEU and TRU, used internally to study all the details of the GALA instrument, have been developed using ESATAN-TMS. The detailed thermal model of the ELU has been developed by Airbus Defence and Space using *Systema*.

4.2.3 Models Correlation

A step of critical importance in the development is the validation and the improvement of the detailed models through correlation with experimental test results. The first correlation for all the three units has been carried out with the results of the thermal balance tests performed on the structural and thermal models (STM). Following thermal vacuum tests with qualification model and the proto-flight model have been used to improve the accuracy of the model predictions.

The main success criteria of the correlation of the detailed models include temperature deviations of max 2 °C at the thermal reference point (TRP), maximum 5 °C for the main structural parts and maximum 10 °C for the MLI and the space-exposed part of the baffle. The requirement about the heat fluxes at the interfaces was a max deviation of 5%. The correlation of the models has been a long but successful task, with the minor exception of the outer section of the baffle: this passive, space-exposed element of the instrument has been designed to cope with an extreme range of temperatures, covering at least the range from −100 °C to +125 °C. For this wide range, a requirement on the accuracy of the correlation of 5 °C has proved to be too tight: in some cases, the deviation has reached 8 to 12 °C, and in a single, extreme case the deviation has reached +22 °C. Since the precise temperature of this external part is not influential for the rest of the instrument, the deviation has been reckoned acceptable.

The reduced models, developed with a limited number of nodes and surfaces in order to speed up coupled analyses, have been numerically correlated with the results of the detailed model, simulating real in-flight scenarios. The same accuracy parameters used for the correlation of the detailed models have been applied for the correlation of the reduced models.

4.2.4 Analyses with the Detailed Models

The detailed models have been used to simulate the complete envelope of the mission, verifying that all thermal requirements are fulfilled. Specifically, all components, parts, materials and coatings are expected to remain within the qualification range including model uncertainties and margins. The phases with the lowest margins have been identified as (1) the launch phase, during which the upper part of baffle approaches the qualification temperature of the coating, and (2) the contingency scenario with sun illumination at Venus, which may result in temperatures close to the worst tested cases for the secondary mirror and the baffle. In both cases, the critical temperatures are expected at surfaces coated with vapor deposited gold which is a very efficient solar absorber. The electronic boxes have proved to be within the thermal requirements with solid margins in all the specified scenarios.

4.3 Radiation Environment

JUICE is a challenging mission, requiring sensitive equipment to survive and operate within the harsh radiation environment at Jupiter. The magnetosphere of Jupiter is dominated by electrons, which have a great penetration depth making it difficult to shield internal components. Due to the very high fluxes, these electrons also induce significant levels of displacement damage, in addition to ionization.

GALA has been synergistically designed, considering both structural and radiation requirements from the very early design phases. In this way, the shielding efficiency has been maximized, optimizing the total mass of the instrument at the same time. Due to this development concept, however, it is not possible to clearly differentiate between shielding mass and structural mass.

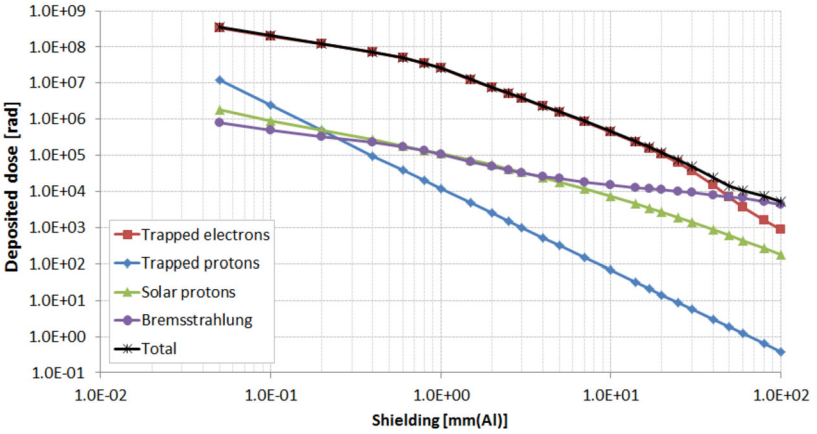

Fig. 3 Total ionizing (TID) dose as a function of shielding depth with Aluminum for ray-tracing analysis

For the JUICE mission, the main contributor to the total ionizing dose (TID) are primary electrons trapped in the magnetosphere. For heavily shielded parts, secondary radiation becomes an important contribution to the deposited dose. Protons from solar events or trapped in the Jupiter magnetosphere play a very minor role. The GALA elements most sensitive to TID effects are the detector, a Silicon Avalanche Photo Diode (Si-APD), the laser pump diodes, the Nd:YAG laser crystals, the energy monitor of the laser, and in general the analogue electronic components.

Displacement Damage (TNID) affects all opto-electronic devices (in particular detectors), materials with crystalline structure and potentially all electronic parts which make use of bipolar technologies. The GALA elements most sensitive to displacement damage are the Si-APD and the Nd:YAG laser crystals.

Single Event Effects (SEE) are typically caused by heavy ions in the Galactic Cosmic Rays (GCR), and secondarily by Solar Particle Events (SPE), mostly protons in the extreme-high energy range. In terms of SEE, the environment at Jupiter is not very different from the environment in any other part of the solar system: the SPEs are weaker than at 1 AU, but this secondary effect is compensated by the slightly higher level of GCRs.

Internal (deep) electrostatic charging is particularly dangerous for large volumes of dielectrics and for metallic parts which are not grounded. The Europa flyby represents the most challenging scenario, with an integral flux of 2.4×10^7 e^- cm^{-2} sr^{-1} s^{-1}.

The radiation-induced noise is a phenomenon which increases the background noise in sensors. The Si-APD of GALA is known to be sensitive to electrons and to low energy photons: therefore, the device may be affected by the primary radiation consisting of trapped electrons but not significantly from the secondary gamma rays.

4.4 Radiation Modelling

4.4.1 Cumulative Effects (TID and TNID)

The first step consisted of a sector analysis with a ray-tracing method. The main goal was to quickly identify the order of magnitude of the radiation doses in different parts of the instrument, before more detailed —and resource-consuming— particle transport analyses would be performed. The TID dose-depth curve (Fig. 3) and the displacement damage were

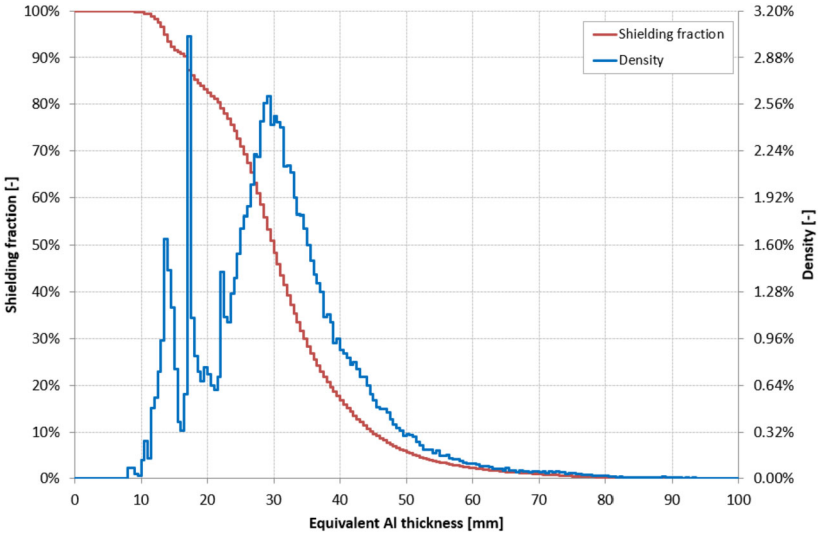

Fig. 4 Example of sector analysis histogram

simulated. The process has been repeated for each of the sensitive parts that needed to be investigated, obtaining from the ray-tracing algorithms a shielding thickness distribution (an example is shown in Fig. 4) and a dose prediction.

The particle transport analyses have been performed both using FASTRAD and GRAS, a tool which exploits the Geant4 toolkit to perform complex analyses maintaining a simple interface. The Reverse Monte Carlo method has been preferred to the Forward Monte Carlo approach due to the significantly lower computational time. The detailed radiation model of the whole spacecraft has been provided by Airbus Defense and Space and integrated with the GALA model for the calculation, since the typical approach consisting of a six-face equivalent thickness specification has been judged insufficient for the detailed particle transport analysis.

After several iterations, the radiation analyses have proved that all electrical and optical parts, all materials and coating are compliant with the required radiation design margin. In particular, it was possible to reduce the dose deposited into the Si-APD below 15 krad(Si) concerning TID and below 6.5×10^7 MeV g(Si)$^{-1}$ concerning TNID.

The radiation tolerance of many electronic components has been taken from existing data-sheets and test reports, but for the custom designed parts of the laser, of the optics, for the detector and for some coatings it was necessary to carry out radiation tests at the predicted mission levels.

4.4.2 Single Event Effects

The Single Event Effects have been mitigated primarily through selection of rad-hard components. In particular, no device has been used with linear energy transfer (LET) tolerance below 60 MeV cm^2 mg^{-1} for destructive or potentially destructive effects: this includes latch-ups (SEL), snapbacks (SESB), gate and dielectric ruptures (SEGR and SEDR) and burnouts (SEB). The MOSFETs included in the system have been implemented so that to always operate within their Safe Operating Area defined at 60 MeV cm^2 mg^{-1} or above.

Concerning non-destructive SEE, it was not possible to find only SEE-free components. For each possible non-destructive effect of each component, a *severity code* from 1 to 5, associated to the impact of the possible event on the system performance, has been derived. Only parts with severity code 1 (negligible or no impact) and 2 (moderate reduction of performance) were included in the final DCL (declared component list). The highest risk has been identified as an upset causing a wrong command to the main electronics unit, resulting in no answer until the command is repeated, with the associated loss of time.

4.4.3 Deep Dielectric Charging

The highest risks were mitigated by design: the use of large dielectric parts was strictly forbidden, as well as the implementation of any non-grounded metallic part. On the other hand, strict requirements concerning electrical grounding have been implemented. The PCBs of the laser and of the electronic boxes were designed minimizing the portions without copper layers, in order to reduce the charge build up in the polyimide volume.

The optical coatings applied on the lenses exposed to deep space, in particular the beam expander, were designed to be electrically conductive and were grounded. The time constant for charge build up in the beam expander has been analytically calculated and verified to be much longer than the duration specified for the associated worst-case electron flux.

The MLI blankets have been designed to include at least one conductive layer, and to have a minimum of two grounding points, located at the opposite corners of the blanket, bonded to the structure with a resistance below 100 mΩ. The internal resistance between the grounding points and the conductive layer was specified as and verified to be below 100 Ω.

4.4.4 Radiation-Induced Noise

The environmental radiation sources can deposit energy in the APD, mimicking the energy deposition caused by the signal photons. A simplified analysis has been carried out both analytically and numerically running a simplified simulation with Geant4.

The analysis considers that the number of electron-hole pairs generated from impinging electrons can be derived from the incident spectrum, the stopping power in the target material, the energy necessary to create a pair and the geometrical chord length distribution of the sensitive volume. The energy deposition rate spectrum has been calculated using the Bradford formula.

The sensitive volume of the APD can be very well approximated with an oblate cylinder, with a diameter of 0.8 mm and a height of 0.13 mm. The probability that an electron in the given spectrum, and intersecting the sensitive volume, deposits at least 3.6 eV is greater than 0.999: basically, any electron reaching the sensor enhances the background noise. Finally, it must be considered that the effect of the enhanced background plays a role only during the observation window of the detector. The return signal of the APD is measured only for a very small fraction of the total time: assuming the nominal laser frequency of 30 Hz and 4000 samples with a duration of 12.5 ns, only 0.15% of the electron-hole generation impacts the SNR.

The results of the analytical and numerical analyses are reported in Table 3: Many of the predicted events generated by electrons would cause extremely large energy deposition, orders of magnitude larger than the signal generated by the photons of the return pulse, making it possible to simply filter out the corresponding measurements.

Table 3 Simulated electron fluxes at the GALA detector

Electron flux	Method	Event rate # s^{-1}	Event rate # laser $shot^{-1}$
mission average	analytical	2.57×10^{-2}	8.57×10^{-4}
Ganymede average	analytical	7.22×10^{-2}	2.41×10^{-3}
	numerical	9.71×10^{-2}	3.24×10^{-3}
worst case	analytical	2.30×10^{0}	7.66×10^{-2}

5 The GALA Instrument

5.1 Instrument Design

The GALA development is based on heritage from the BepiColombo Laser Altimeter (BELA). Descriptions of BELA are given in Thomas et al. (2021). A previous overview on GALA before completion of the flight-model is given in Hussmann et al. (2019). GALA uses a pulse repetition rate of 30 Hz nominal (48 Hz maximum over specific topographic features), which was required for keeping the interpolation error at cross-over points (crossing laser tracks at Ganymede's surface) sufficiently small for the error budget of the tidal measurements and for obtaining sufficient along-track coverage at close —and thus fast— flybys. The bandwidth of the GALA detector is 100 MHz. With a sampling rate of 200 MHz for the pulse digitization, this will allow for improved characterization of the return pulse shape, which will provide invaluable information on roughness and reflectivity of Ganymede's icy surface. At an altitude of 500 km of the circular Ganymede orbit, GALA uses a laser pulse energy of 17 mJ for generating sufficient return pulse energy.

The GALA design is compact to take advantage of shielding by mechanical parts in addition to spot shielding that was necessary for exposed components of the transceiver unit. Specific materials have to be used e.g. for the optical components to avoid darkening due to radiation effects. For JUICE, the electronic boxes are located inside a spacecraft vault together with electronic boxes from other instruments and are, therefore, located quite remotely from the optical unit. A particular challenge is the qualification of optical components of the transceiver system. Therefore, extensive electron irradiation testing has been performed with the optical and electro-optical components of the GALA transceiver system. A baffle system handles the different thermal and stray-light conditions during the cruise phase towards Jupiter and during the mission phase.

The model philosophy of GALA consisted of three models. The electrical model (EM) that can be fully commanded (including laser firing) and is used for full-functional tests. It is mounted on the EM of the JUICE spacecraft, located at ESOC (Darmstadt, Germany), and supports preparation of operation sequences. The structural thermal model (STM) was used for representative mechanical testing and thermal cycling. The proto-flight model (PFM) is mounted on the JUICE spacecraft. For several sub-units, engineering qualification models (EQMs) were built which have seen substantial testing for verifying the functionality and robustness of these units. Flight-spares (FS) do exist for the electronic units ELU and LEU (see below), the optical receiver assemblies and relevant parts of the TRU. They are assembled as functional-representative Ground reference Model (GRM), which serves as instrument software development and test facility on ground during the cruise and mission phase.

The GALA instrument consists of three units which incorporate several sub-assemblies (see Figs. 5, 6 and 7):

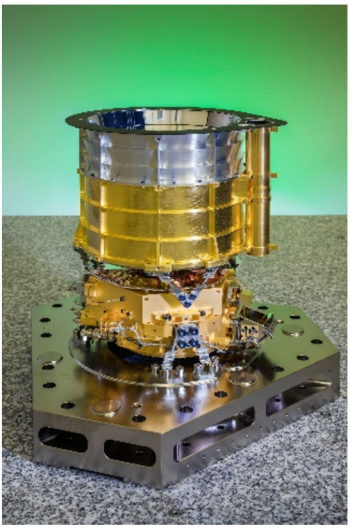

Fig. 5 The GALA Transceiver Unit (TRU) Flight Model (outer MLI not installed, Image Courtesy: Hensoldt Optronics)

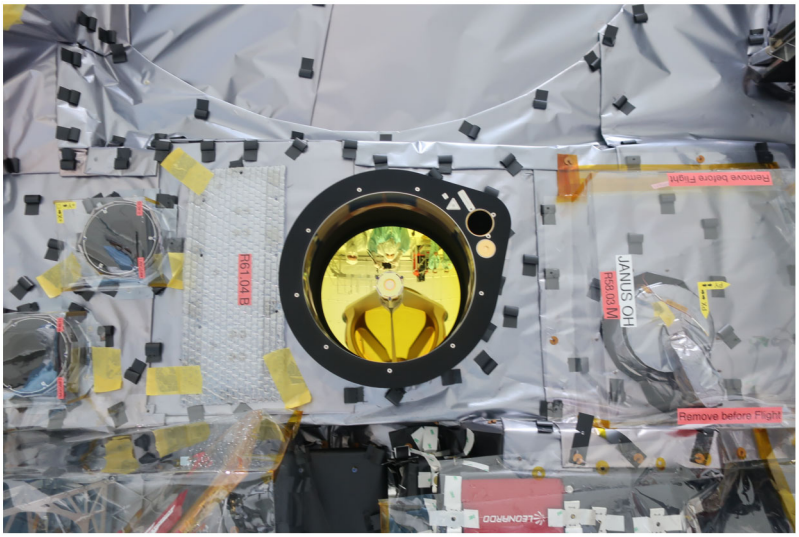

Fig. 6 The GALA Transceiver Unit (TRU) Flight Model mounted on the JUICE spacecraft. The GALA receiver telescope and the baffle are clearly visible, the aperture for the outgoing laser beam is top right to the telescope. Left to the TRU are the two JUICE navigation cameras, right to the TRU is the JANUS camera

1. The Transceiver Unit (TRU) (Fig. 5) houses the laser optics (Laser Head Module, LHM) and the appropriate laser head electronics. After leaving the laser housing, a tilt mirror guides the laser pulse towards the moon's surface. The return laser pulse is received by the receiver telescope (TEL) and focused on the detector (Si-APD) by the back-end optics (BEO). The Analog Electronics Module (AEM) pre-amplifies and digitizes the detector output before it is directed to the Range Finder Module (RFM) inside the Electronic Unit (ELU). The TRU includes a baffle that protects the receiver telescope against straylight from Jupiter's atmosphere, from surface reflections from the target outside the laser foot-

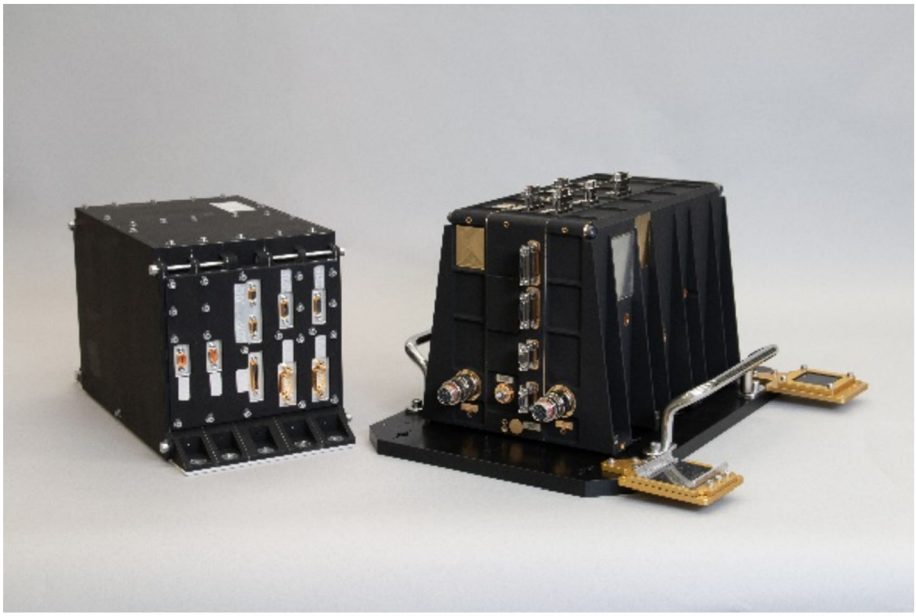

Fig. 7 The GALA Electronics Unit (ELU) and the Laser Electronics Unit (LEU) flight models

print, and from reflection of light by other parts of the spacecraft. The baffle furthermore prevents laser straylight from direct incidence to the receiver telescope and from hitting other parts of the spacecraft.

2. The Electronic Unit (ELU) houses the digital rangefinder module (RFM), which analyzes the detector signal and computes range, and pulse shape for the analysis of surface slope and roughness. The Digital Processing Module (DPM) is the main computer of the instrument and controls all instrument functions as well as the interface to the spacecraft. The Power Converter Module (PCM) provides power in different voltages for all instrument assemblies.
3. The Laser Electronics Unit (LEU) consists of the laser control module, the laser diode driver, and the power distribution module. These include capacitors, high-voltage supply, and power driver for the laser pump diodes.

Electrical interfaces to the spacecraft for power, data and precise time reference are routed through the Electronic Unit. Thermal interfaces to the spacecraft are realized with spacecraft-provided heat pipes, conductive surface contacts to the spacecraft panel, and the three units outer surfaces to the spacecraft (radiative).

The instrument is equipped with electrical heaters that keep the TRU in its non-operation temperature range, avoid cold traps at sensitive optics to restrict contamination build up and that will go to higher temperature levels for decontamination of optical surfaces.

Mechanically, the two electronic units are bolted on the spacecraft panel on top of the heatpipes. The TRU uses stress-free bipod-mounting that ensures the required pointing stability throughout the mission. The GALA flight model consumes 50.6 W in standard science mode (17 mJ at 30 Hz) and has a mass of 23 kg including harness. Key characteristics of the GALA instrument are listed in Table 4.

Table 4 Key characteristics of the GALA instrument

Parameter	Value
Laser energy	17 mJ at 30 Hz
	8 mJ at 48 Hz
Pulse Repetition Rate	30 Hz, 48 Hz
Wavelength	1064.5 nm
Pulse Width (30 Hz, full width at half maximum)	5.5 ns
Beam Divergence (full cone at $1/e^2$ intensity)	100 μrad
Receiver Telescope Radius	12.5 cm
Receiver Field of View (full cone)	580 μrad
Mass (including shielding and harness)	23 kg
Power (in nominal science mode)	50.6 W

Some assemblies of the instrument are in cold redundancy. These are the DPM and the PCM inside the ELU, the laser electronics inside the LEU and the lasers inside the LHM (see below).

5.2 The Laser System

5.2.1 The Laser Head Module (LHM)

The LHM is part of the TRU and consists of (1) a diode pumped cavity with a laser crystal (Nd:YAG) which is side-pumped by two laser diode arrays, (2) an electro-optical Q-switch (Pockel's Cell) which triggers the generation of the required short pulses, and (3) optics for an unstable laser resonator with a graded reflectivity out-coupling mirror enabling low transversal mode operation with near diffraction limited beam quality of $M_2 < 2.3$. The mechanical/thermal design of the laser resonator includes a three-stage decoupling configuration of the laser resonator from the LHM to get a stable running laser source under mechanical and thermal operating conditions. The actual laser resonator consists of three mirrors —end mirror, folding mirror, out-coupling mirror— and two wave plates which are directly mounted at the laser resonator bench. As far as possible, the laser resonator bench is thermally and mechanically decoupled from the rest of the LHM, i.e., there is no direct heat dissipation from either the laser diode arrays or the laser rod into the laser resonator bench. Mechanically, the laser resonator bench has four small bolt areas as an interface to the transmitter optical bench to get an optimum thermal isolation from each other. All other laser resonator optics (polarizer, laser rod, and Pockel's cell) except the laser diode arrays were mounted directly to the transmitter optical bench. The transmitter optical bench also provides a stable platform for the remaining beam guiding optics outside the laser resonator. Also the transmitter optical bench only has three mechanical interfaces to the base unit. Therefore, it is similarly decoupled from the base unit as the laser resonator bench from the optical bench.

The pump laser diode arrays are operated with 200 A laser diode current and are therefore the most intense heat sources inside the laser resonator. They are directly mounted on the LHM. From the LHM, the heat is removed via the transmitter cover and the thermal strap to the spacecraft cold finger interface. The conduction cooled cavity design consists of the Nd:YAG rod, which is side pumped, the related housing, and mounting pieces. The predefined size of the LHM requires a small package of the laser rod unit optimized for high efficiency and a wide operational temperature range.

5.2.2 The Laser Electronics Unit (LEU)

The laser electronics unit (LEU) (Fig. 7) contains all laser electronics and controls all laser operations:

- Laser diode drivers, main, and redundant.
- Laser control module.
- Power distribution module.

It has a data interface to the electronics unit (ELU), but no direct electrical interface to the spacecraft. The LEU generates high pump current (200 A) for the laser pump diodes inside the LHM. It contains capacitor reservoirs for providing the laser pump energy. Inside this electronics box, different sub-assemblies are mounted in frames, which are mated together to form the LEU. The LEU is accommodated in close vicinity to the TRU, since the harness length of the laser power cables should be kept below 0.5 m. The high-power electronics circuits are separated from the sensitive signal electronics into different compartments and into secondary circuit groups with separated grounding references. This reduces the cross-talk from the high-power electronics of the laser system to low-noise electro-optical sensor electronics needed for processing the APD signal or the energy monitoring of the laser pulse, or any precise control voltages such as temperature sensor read-outs. In addition, the phase margins of receiver amplifiers or the servo-loops for the voltage level controls have been analyzed and measured carefully in order to improve their robustness against electro-magnetic interference.

5.3 The Receiver Telescope and the Baffle

The TRU includes a baffle that protects the receiver telescope against straylight from Jupiter's atmosphere, from surface reflections from the target outside the laser footprint, and from reflection of light by other parts of the spacecraft. The baffle furthermore prevents laser straylight from direct incidence to the receiver telescope and from hitting other parts of the spacecraft.

The baffle is a lightweight aluminum structure, divided in two parts. The lower part, surrounding the telescope, has a flat surface and is coated with Acktar Fractal Black. It provides a homogeneous thermal environment to the telescope structure. The upper part is a Stavroudis-type baffle. The shape is a sequence of sections of hyperboloids and ellipsoids with the goal to reject incident radiation with as little baffle-internal reflections as possible. That part of the baffle is gold coated.

The optical design of the TEL comprises two mirrors (first mirror M1 and secondary mirror M2), which form a Ritchey–Chretien telescope with a focal length of 1200 mm. The back focal distance is positioned at 10 mm of the vertex to the intermediate image plane behind the M1 apex. The free entrance pupil diameter, respectively, the effective receiver diameter of at least 250 mm, is equivalent to the un-obstructed area of the mirror M1. The transmission of the receiver telescope into the field stop aperture is influenced by the reflectivity of the mirrors at 1064 nm, various alignment errors in addition to image blur. The total reflectivity of the telescope mirrors will be at least 95% (begin of life). The resulting optical transmission including the effects of these deviations but without degradation effects caused by contamination and/or particles will be at least 86%. The end-of-life optical transmission of the telescope is budgeted with 83%. The receiver field of view (full cone) is fixed by the diameter of the field stop aperture and the focal length of the telescope. The value is limited to less than 580 μrad including all manufacturing and assembly tolerances as well as

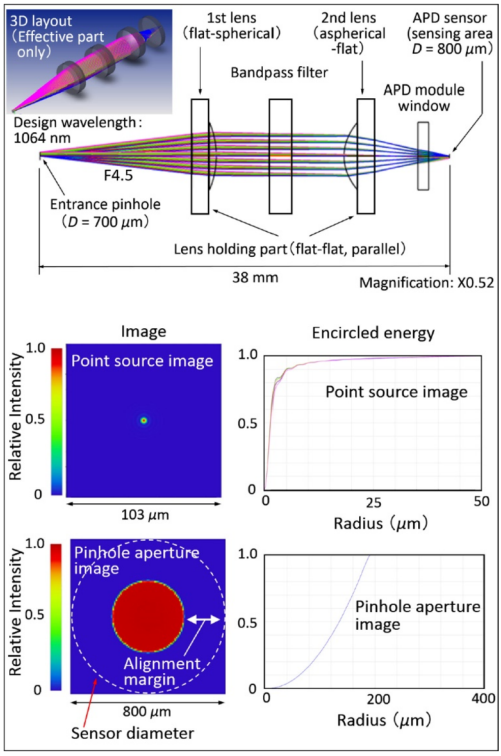

Fig. 8 Back-End Optics (BEO) optical design. Top: design of the lens optics (APD: Avalanche Photo Diode); bottom: imaging properties (Enya et al. (2021), https://doi.org/10.1016/j.asr.2021.11.036)

environmental loads. The transmitter has a beam divergence of 100 μrad. The receiver has to capture the return pulse, i.e., its field of view must be larger than the beam divergence and the alignment between transmitter and receiver must be stable. The value of 580 μrad for the receiver field of view accounts for the beam divergence and includes margins for cross-alignment and thermo-elastic distortions.

All materials for the telescope are selected to provide sufficient radiation hardness against high-energy radiation (electrons, protons, and gamma rays) to the levels experienced at the telescope during the mission. The material of the mirrors M1 and M2 together with the reflective coating in combination with the strut material is chosen for optimum adaption and athermalization to ensure the optical performance over the operational temperature range.

5.4 The Back-End Optics (BEO)

The back-end optics (BEO) module is installed between the receiver telescope and the focal plane assembly (FPA) within the GALA TRU. The BEO performs spatial and wavelength filtering to detect return pulses with an adequately high signal-to-noise ratio (SNR). Figures 8 and 9 show the optical and mechanical designs of the BEO, respectively, in conjunction with the FPA. Enya et al. (2021) provide comprehensive details about the BEO.

With a 700 μm diameter pinhole, the entrance aperture of the BEO is positioned at the focal point of the receiving telescope, acting as a spatial filter for return pulses. The f-number of the light after passing through the pinhole is 4.5. Within the BEO, the first lens collimates the return pulses, facilitating precise wavelength filtering through a band-

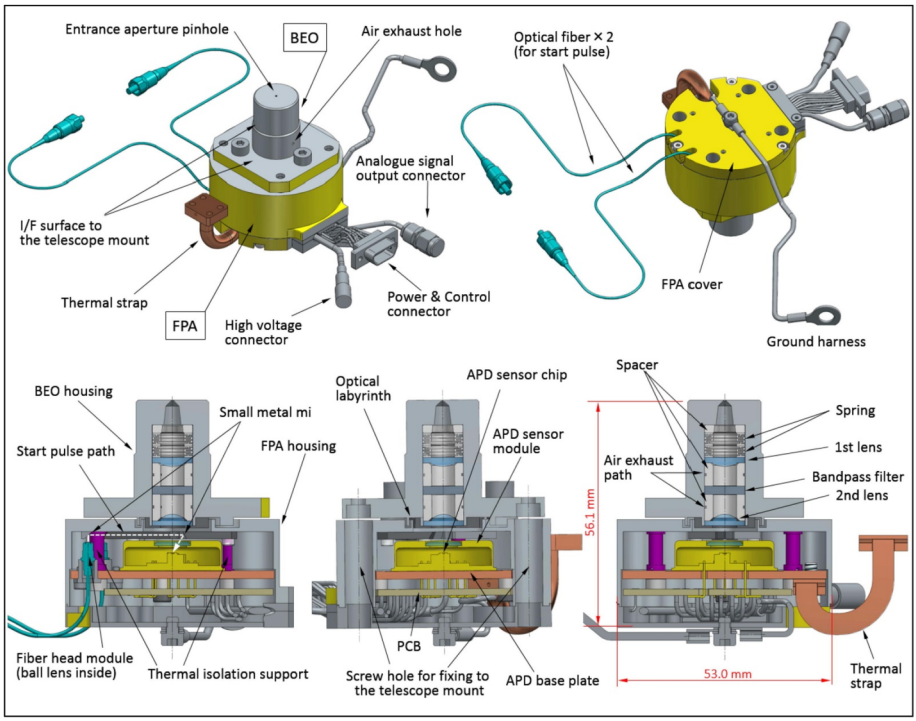

Fig. 9 External (top) and cross-section (bottom) views of Back-End Optics (BEO) and Focal Plane Assembly FPA (Enya et al. 2021)

pass filter. Subsequently, the second lens reconstructs the focal plane image, as illustrated in Fig. 8.

Quartz is used as lens material in the BEO, enhanced with an anti-reflection coating on the surfaces. The optical design of the BEO incorporates only two lenses to maximize the throughput. These optics function as a reduction lens with a magnification factor of 0.52, thereby enhancing the alignment tolerance with the FPA. The implemented anti-reflection coating demonstrated a reflectivity of 0.05% or less per surface, notably below the 0.5% requirement.

The bandpass filter, as shown in Fig. 10, exhibited an average transmissivity of 96% (exceeding the requirement of 90%) across the mandated transmission wavelength range of 1064.53 ± 1.5 nm. The measured optical density (OD) of the bandpass filter was more than six (requirement: 5) in the blocked wavelength range of which the lower and upper wavelength limits were 300 and 1200 nm, respectively (Fig. 10).

The housing of the BEO interfaces with the receiver telescope with high precision. The BEO housing was crafted from a single SUS316 stainless steel block using high-precision machining techniques, and then surface passivation treatment was applied to the BEO housing. Segments of its external surface were gold coated to diminish the thermal emissivity, as shown in Fig. 9. In the BEO, an air path was created to allow the air inside the housing to escape during launch. To prevent the ingress of stray light, the air path was designed to transmit through multiple bends.

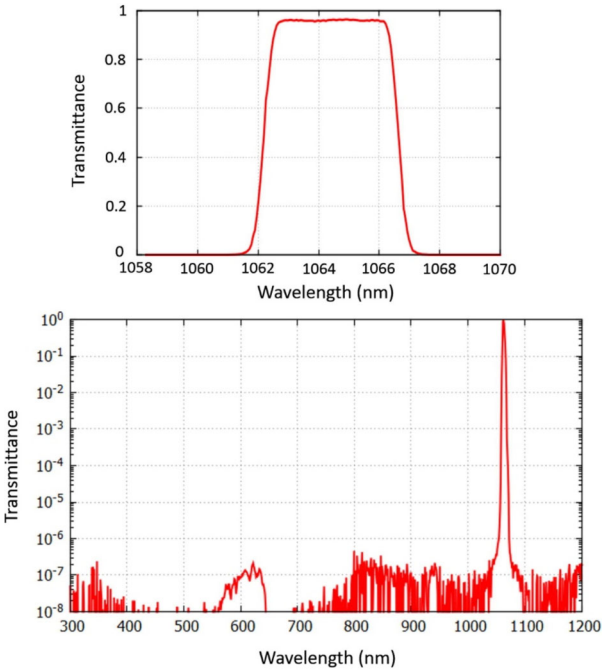

Fig. 10 The measured transmittance of the bandpass filter is 96% with a center wavelength of 1064.53 ± 1.5 nm (Enya et al. (2021), https://doi.org/10.1016/j.asr.2021.11.036)

5.5 The Focal Plane Assembly (FPA)

The FPA contains the avalanche photodiode (APD) sensor module, which includes the APD sensor and its associated devices, as shown in Fig. 9. The Flight Models of the BEO and FPA are shown in Fig. 11. The primary function of the FPA is to convert the optical signal, comprising both the return pulse and a segment of the start pulse, into an electrical signal (see Enya et al. (2021) for comprehensive details).

The return pulses are channeled into the FPA from the BEO and incident on the APD sensor. To introduce a fraction of the start pulse, the FPA incorporates two redundant optical fibers. This design enables the detection of the time lag, intensity ratio, and pulse width broadening of the return pulse relative to the start pulse by using the same detector. These fibers are the RadHard 62.5/125-micron Multimode Fiber (MIL-PRF-49291/6), produced by DRAKA, and characterized by a numerical aperture of 0.275, cladding diameter of 125 μm, and core diameter of 62.5 μm.

The start pulses transmitted to the FPA via optical fiber initially traverse a small ball lens to reduce the beam diffusion angle. Subsequently, the beam is bended by reflecting surfaces twice before reaching the APD sensor. Because space constraints within the FPA precluded the installation of standard mirrors, the reflecting surfaces to work as mirrors were realized as part of an internal structural component by polishing and gold-coating segments of the structural component.

The output signal of the APD sensor is amplified by a transimpedance amplifier (TIA) with a bandwidth of 100 MHz in the APD sensor module. The APD sensor module for GALA was developed from a commercially available product by Excelitas Technologies Corp., LLAM-1060-R8BH, which was redesigned and underwent qualification testing to satisfy the performance criteria of GALA and the environmental tolerances required for the JUICE mission. Although the APD sensor is a commercial product, it was carefully

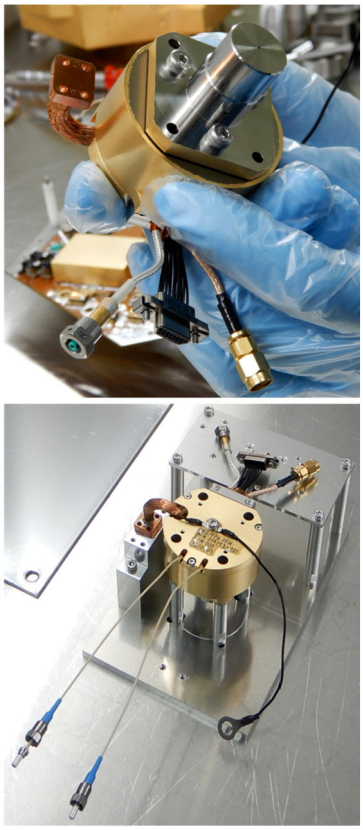

Fig. 11 Flight Model of the Back-End Optics (BEO) and the Focal Plane Assembly (FPA) (Enya et al. (2021), https://doi.org/10.1016/j.asr.2021.11.036)

selected from a manufacturing lot controlled for GALA development, ensuring compliance with specific requirements. Additionally, the TIA, integrated into the APD module as a pre-amplifier, was custom-designed and manufactured to satisfy the bandwidth, gain, and noise level specifications.

The GALA-utilized APD sensor, derived from C30954E Si-APD, shows a high quantum efficiency of 0.41 at the fundamental wavelength of YAG lasers (1064.5 nm). The corresponding responsitivity at unity gain at 25 °C was determined with 0.352 A/W. With the nominal bias voltage of 346 V, the responsivity is at 685.4 kV/W. The breakdown voltage of the selected flight APD is at 385.5 V. This type of sensor has been successfully deployed in several space missions, notably in LALT on the Kaguya mission (Araki et al. 2009) and LIDAR on the Hayabusa 2 mission (Mizuno et al. 2017).

In the development of the APD sensor module, a significant challenge was the performance degradation induced by high-intensity electron beams in the Jovian magnetosphere. To assess the radiation tolerance of the APD sensor, an electron beam irradiation test was conducted at ONERA, the French Aerospace Lab. In addition, proton irradiation tests were performed at the radiation laboratory of the National Institute for Quantum and Radiological Science and Technology in Japan, as well as the cobalt irradiation facility at Tokyo Institute of Technology, Japan.

5.6 The Analogue Electronics Module (AEM)

Figure 13 depicts the AEM, a circuit board with two sets of flat cables, to be built in the TRU housing serving as the optical bench for GALA's receiver telescope.

The AEM plays a crucial role for converting the APD sensor's analog signal (with a 100 MHz bandwidth and continuous temporal variations) into real-time digital data using an ADC circuit. The processed data is then sent to the Range Finder Module (RFM). To ensure there is no degradation in the output signal of the APD module, an analog signal line that incorporates a gain control amplifier and a differential conversion circuit was designed. This line directs the APD output signal to the ADC circuit. As a result, the noise level of the input signal to the ADC was measured at 39 fW/$\sqrt{\text{Hz}}$ at NEP, and the noise at the APD output signal was measured at 27 fW/$\sqrt{\text{Hz}}$ at NEP. These performances met the specified requirements of GALA. The requirements were also satisfied for the gain flatness of ± 0.5 dB across the entire bandwidth from 100 kHz to 100 MHz. The AEM provides two set-points for the APD gain: one for the Tx start pulse, one for the Rx return pulse. The Tx start pulse – a fraction of the outgoing laser pulse routed through the optical fiber – contains a comparable strong optical signal and requires a low APD gain of -3 dB (at 100 MHz relative to 400 kHz) in order to not saturate the APD. The Rx return pulse on the other hand has a higher gain of 14.7 dB in order to generate a suitable analogue output signal. The correct timing of the gain-switching is controlled by the DPM in connection with laser pulsing and range gate setting.

The ADC circuit employs two 100-Msps ADCs and samples the waveform of the APD sensor signal at 200 Msps with 12-bit resolution using a time-interleaved method, where the sampling timing of each ADC is shifted by 180°.

The AEM's additional role is to optimize the APD sensor module for pulse measurements. It features a controllable high-voltage circuit (300–400 V in 1 V steps) for applying reverse bias to the APD sensor, enhancing its responsivity. The AEM includes a thermal control circuit, utilizing a Peltier device to stabilize the signal gain by controlling the APD sensor's temperature, as temperature strongly influences sensitivity.

The functional block diagram of the AEM is shown in Fig. 12. The outputs of the two ADCs (ADC0 and ADC1) are transmitted to the RFM through two connectors synchronously as 24-bit data with a 100 MHz clock frequency (Enya et al. 2021).

5.7 The Range Finder Module (RFM)

A laser altimeter fires a short laser pulse (*Tx pulse*) towards a target and searches for scattered photons (*Rx pulse*) that make their way into the receiver and onto the light sensitive surface of an avalanche photo diode (APD). The analogue output of the APD is digitized by the AEM (cf. Chap. 5.6) and sent to the RFM. A small fraction of the light of the outgoing Tx pulse is routed onto the same APD as the Rx pulse. The time of the Tx pulse and the Rx pulse is measured against the same clock, and the difference is associated with the distance, making use of the constant and well-known speed of light, c.

In order to constrain the chances of detecting erratic pulses, a rangefinder searches for the Rx pulse only in a sufficiently large (i.e. long) but, still small compared to the distance, time interval in which the Rx pulse is expected. This time interval is called *range window* or *range gate*. A digital rangefinder —as opposed to analogue rangefinders such those used in MOLA, LOLA, and MLA— uses digital samples of the range window, and searches for a transmitter and a return pulse by comparing samples with a pre-described subset of samples that are believed to match the shape and width of the return pulse. The pre-described filter

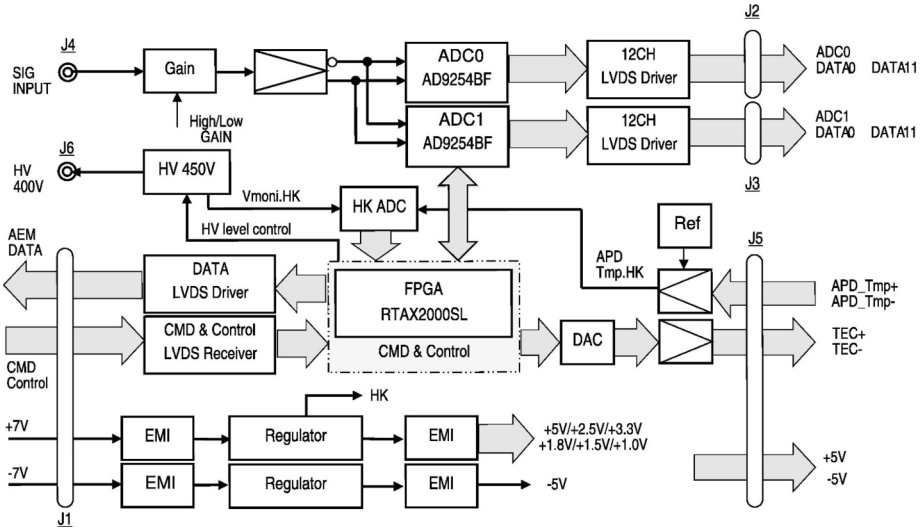

Fig. 12 Functional block diagram of the AEM. Complete expressions of the abbreviations used in the diagrams are stated as follows: ADC: Analog-to-Digital Converter; CMD: Command; DAC: Digital-to-Analog Converter; EMI: Electromagnetic Interference filter; FPGA: Field Programmable Gate Array; HK: Housekeeping data; HV: High-Voltage supply; LVDS: Low-Voltage Differential Signaling; $V_{moni.HK}$: Voltage monitor Housekeeping data (Enya et al. (2021), https://doi.org/10.1016/j.asr.2021.11.036)

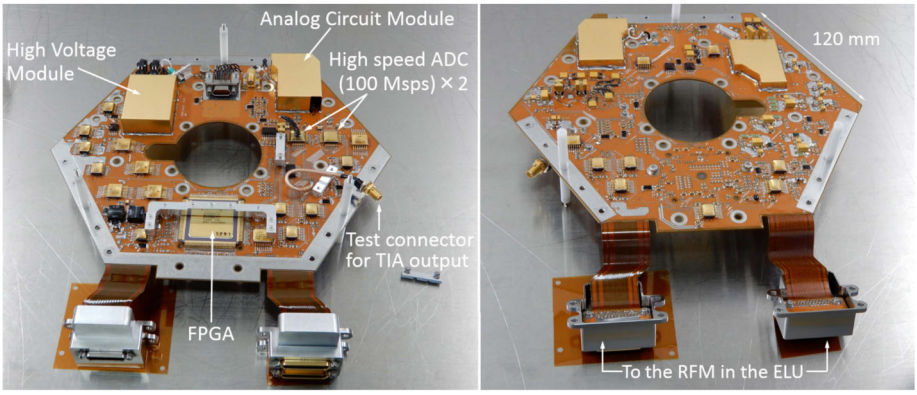

Fig. 13 External appearance of the Analog Electronics Module (AEM); ADC: Anolog-Digital Converter; TIA: Trans-Impedance Amplifier; RFM: Range Finder Module; ELU: Electronics Unit (Enya et al. (2021); https://doi.org/10.1016/j.asr.2021.11.036)

must be scaled to match a wide range of pulse durations. The original, short Tx pulse might hit a tilted or rough surface, which means that not all photons travel the same distance. This leads to a pulse widening which must be accounted for. At the same time, the Rx pulse width is a measure for surface roughness or slope, and is also of scientific interest. Therefore, the digital rangefinder must return the width to which the matched filer has to be scaled/broadened to give the best fit. Likewise the matched filter must be scaled with respect to its intensity in order to match bright and weak Rx pulses. Again, the intensity of the Rx

pulse contains interesting scientific information, i.e. the reflectivity (albedo, brightness) of the target material. Therefore, the rangefinder must return this value in its science data.

Because a digital filter needs to be scaled and broadened in order to match bright and weak, narrow and wide Rx pulses, it is often referred to as a *filter family*, described by the same set of samples plus a scaling and broadening parameter. A filter family can be described by a set of polynomials (*basis functions*) and associated coefficients, which synthesize the digital filter. A digital rangefinder can use more than one filter family at the same time, each described by their own set of coefficients. The filter coefficients can then be used to compute the matched filter, consisting of sufficient *samples* to cover the widest required Rx pulse at the nominal sampling frequency. The actual shape of the used filter families, i.e. their coefficients, can be modified by command, i.e. they are not hard coded. This is the basis for the GALA RFM.

The rangefinder is fed with digital samples from the AEM. The rangefinder also receives a set of parameters that control the details of how the range detection is performed. This set of inputs comes from the Digital Processing Module (DPM).

It is critical to ensure that the time interval between the Tx pulse and Rx pulse is always, i.e. under all mission conditions and over the whole nominal mission duration, measured against the same time base. This is achieved by:

- Using an ultra-stable fast oscillator that provides sufficient clock frequency stability on typical time scales for one Tx-Rx cycle, which is the time of flight of a laser pulse from the instrument to surface and return. Usually, such clocks are stable and precise on short timescales, but show significant drift in longer timescales, such as weeks.
- The rangefinder will have a dedicated physical clock signal from the spacecraft's on-board clock. This signal is often called PPS (*pulse per second*) and is created once per second. The spacecraft on-board clock typically shows a large jitter on short timescales and can therefore not be used for the time-of-flight measurement of the laser pulse, but they are very stable over long periods of time.
- The RFM has a register in which the clock count of its internal ultra-stable oscillator is saved each time when it receives a PPS. The register will not be reset on each PPS but is allowed to roll-over. A second register counts the number of PPS ticks that had been received while the first register has been maintained. The comparison between both registers allows for an on-ground post-facto oscillator calibration.

For the GALA RFM, the oscillator is part of the RFM, but the AEM must receive this clock through a dedicated interface. It is used to drive the analogue to digital conversion on the AEM. The RFM records the spacecraft PPS signal to correct the long-time drift of its own oscillator. The RFM does not actually correct the drift; it is corrected on-ground with information provided by the RFM.

When rangefinding, the RFM processes the samples and searches for pulses. This is the nominal operational mode and is called *pulse detection mode*. The rangefinder applies the matched filter algorithm to the Tx samples and detects the Tx pulse and its characteristics such as intensity and width (= duration). It uses only one filter family for this task, because it can be assumed that the Tx pulse shape is well-known, and covered by a pre-determined matching filter family.

The rangefinder applies the matched filter algorithm to the Rx samples and detects the Rx pulse and its characteristics such as intensity and width. Note that the filter vs. samples matching can and usually is performed on sub-sample resolution. This provides a better time resolution, i.e. instrument precision, than the sampling frequency. The RFM uses all (i.e. four) filter families for this task. The rangefinder keeps a list of four Rx pulse candidates

and their associated data. This list can be filled after different rules, such as *one pulse per filter family* or *the best four matches* regardless their filter family.

The rangefinder can deliver a considerable amount of information to the DPM for each laser pulse. This can include:

1. The Tx pulse time with respect to the Tx range window start.
2. The Tx pulse width and intensity.
3. Raw samples around the detected Tx pulse centroid.
4. Four Rx pulses, each with filter family, width and intensity. Alternatively, instead of width and intensity, the rangefinder may return the basis function coefficients that provided the best fit for the detected pulse candidate.
5. For each Rx pulse, raw samples around the detected centroid.
6. A measure for the noise in the range window, i.e. by summing up all samples and dividing by the number of samples (average value), plus the standard deviation.
7. The PPS-clock registers.

Other modes are also available. The most important scientifically is the albedo mode. In this mode, the RFM does not wait for or process a Tx pulse, and it does not search for an Rx pulse. It can be used to determine the surface reflectivity within the telescope's field of view, when used above the dayside of Ganymede. This mode is also a diagnostic mode that is needed for AIV for APD health and performance diagnostics.

The RFM hardware was produced in Switzerland by Syderal under contract to Thales-Alenia Space Switzerland.

5.8 The Digital Processing Module (DPM)

The GALA Data Processing Module (DPM) acts as processor module between instrument subsystems and the spacecraft. The main and redundant DPM's are located together with the Power Converter Module (PCM) and the Range Finder Module (RFM) in the Electronics Unit (ELU). The DPM will perform the following tasks:

- Reception of telecommands and their decoding,
- Reception and processing of the digitized receiver signal,
- Control of the sensor operation,
- Telemetry formatting and transmission,
- Optional data compression,
- Housekeeping data acquisition,
- Instrument health check,
- Software upload support.

The DPM consists of the following devices, depicted in Fig. 14:

- Rad-hard GR712RC dual-core processor including Triple Modular Redundancy (TMR) and EDAC (Error Detection and Correction) against SEU (Single Event Upset) errors, including SpaceWire interfaces to the spacecraft and the rangefinder module,
- Rad-hard Microsemi RTAX FPGA with interfaces to all subsystems,
- 128 MByte SDRAM (Synchronous Dynamic Random-Access Memory) for processor program and data,
- 2 MByte MRAM (Magnetoresistive Random-Access Memory) for Application Software,
- 64 kByte PROM (Programmable Read-Only Memory) containing the Primary Boot Software (PBS),

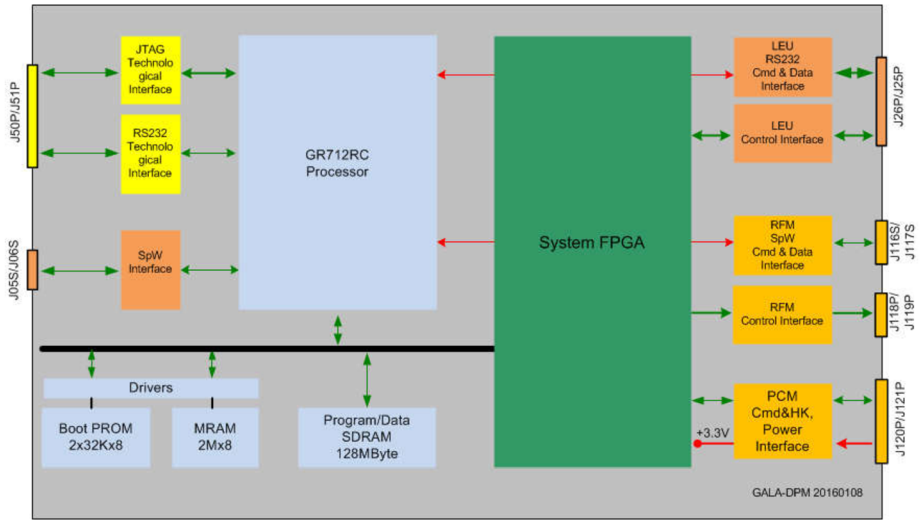

Fig. 14 The GALA Digital Processing Module (DPM). Abbreviations are defined before the reference list

- LVDS (Low-Voltage Differential Signaling) drivers,
- LDO/POL (Low Dropout Regulator/Point of Load) converter and radiation hardened buck regulator to generate needed lower voltages from 3.3 V input.

Communication from the main and redundant DPM as well towards the spacecraft and the rangefinder module is via 100 MBit/s full duplex SpaceWire.

The interface between DPM and the laser subsystem consists of a dedicated laser trigger interface and a serial communication interface for control and housekeeping. The main and redundant DPM are connected with the corresponding main and redundant Laser Control Module (LCM) of the Laser Electronics Unit (LEU).

5.9 The Power Control Module (PCM)

The GALA instrument has been meticulously engineered for optimum functionality, adhering to specified voltage parameters established by the spacecraft's Power Conditioning and Distribution Unit (PCDU). These parameters, applicable to both primary and redundant power lines, dictate a minimum operational voltage of 26.5 V with a tolerance of -3% and a maximum voltage of 28.5 V with a tolerance of $+1\%$. This operational envelope extends across a temperature range from -20 °C to $+50$ °C.

While the Power Converter Module (PCM) is designed to operate seamlessly within the prescribed voltage range, it exhibits adaptability to a broader voltage spectrum, ranging from 22 V to 31 V. This expanded operational range ensures compliance with derating limits for all internal components, thereby maintaining the stipulated output voltages. It is crucial to note, however, that when operating beyond the nominal range, the assurance of compliance with Electromagnetic Compatibility (EMC) requirements and dynamic behaviour cannot be guaranteed.

In instances where the operational voltage falls below 22 V, a protective mechanism prevents the initiation of the DC/DC converter, rendering the module in a secure state with minimal power consumption. Normal module operation resumes promptly upon the restoration of the input voltage to the valid operating range.

5.9.1 The Power Control Module: General Description

The Power Control Module (PCM) is a crucial component of the system. It has input filters tailored to the spacecraft power lines. Two DC/DC converters which are meticulously designed to provide the essential secondary voltages for optimal instrument functionality. There are control electronics circuits built around an FPGA. These circuits operate the power converter and collect its telemetry data. In accordance with the specified specifications, two identical PCMs – main and redundant – have been instantiated in a cold redundant configuration. These modules possess the capacity to be individually powered from the spacecraft through distinct power connectors. The primary role of the PCM is to effectuate the isolation of the spacecraft's primary power bus from the concurrently generated secondary voltages. Noteworthy is the PCM's superior efficiency in secondary power generation, surpassing the threshold of 75%. This efficiency is attained through a custom-designed input filter that precisely regulates the inrush current, limiting it to 1 A/μs.

Further addressing isolation requisites, the PCM ensures galvanic isolation, introducing a configuration of $C > 50$ nF in parallel with $R < 1$ MOhm when the bonding stud is disconnected from a star point grounding system. This provision is essential for achieving compliance with stringent isolation standards in aerospace applications.

The operational mechanism of the Power Conditioning Module (PCM) can be expounded as follows: Initially, the DC/DC converters within the GALA PCM receive power from a linear source connected to the input power bus. Upon initiation, the linear power source yields precedence to a switched power source generated from the primary DC/DC converter transformer to enhance operational efficiency. Concurrently, with the establishment of the 28 V spacecraft bus, the primary DC/DC converter of the GALA PCM initiates autonomously, providing power to all electronic components within the GALA PCM. The activation or deactivation of the auxiliary DC/DC converter is judiciously governed by the Field-Programmable Gate Array (FPGA) in accordance with the prescribed instrument operating mode.

Electrical Block Diagram Description The functional block diagram presented in Fig. 15 is intended to illustrate the operation of the power converter module, showing inter-function relationships, sequential processes and signal paths.

The following points shortly describe the various functions encapsulated within each electronic sub-block:

- PCM Power converter electronics: The power converter interfaces with the S/C 28 V power bus and is responsible for generating the isolated secondary voltages required to operate the GALA electronics.
- PCM FPGA: The custom digital logic functions required by the PCM electronics are built into the FPGA control block. The functions covered in this block are:
  - Primary converter voltage and current telemetries acquisition (+3.35 V and +/−12 V lines).
  - Primary converter over-voltage and over-current management (+3.35 V and +12 V lines).
  - Auxiliary converter voltage and current telemetries acquisition (+7.0 V and −7.0 V lines).
  - Auxiliary converter over-voltage and over-current management (+7.0 V and −7.0 V lines).
  - Board temperature telemetry acquisition

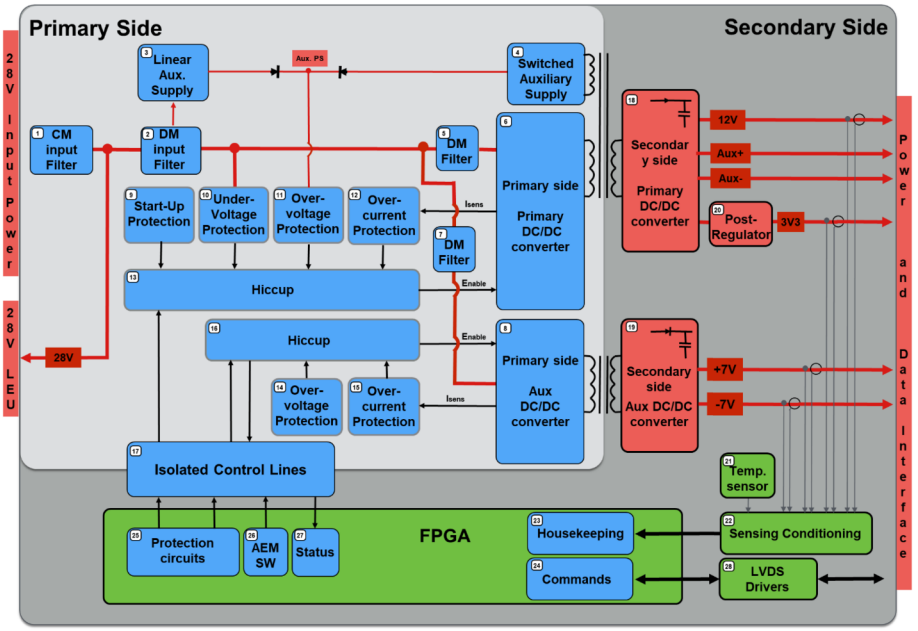

Fig. 15 PCM functional block diagram. Abbreviations are defined before the reference list

  - Primary and Auxiliary converters ON/OFF control and status monitoring for Auxiliary converter
  - Communication with DPM management via LVDS link.
- PCM protection circuitry: The electronics in this block handle all the PCM signals for monitoring the correct operation of the power converter. Special actions are required in the event of overcurrent and overvoltage situations.
- Reset Circuitry: This block is responsible for generating the main reset signals to provide an initial state for all the digital electronics on the board.
- Housekeeping Telemetry and Commands Electronics: As all the control circuitry is built around the FPGA and is tightly linked to control the operation of all the PCM hardware blocks, this block has been designed to collect telemetry data, including voltages, currents and multiple system temperature points.
- LVDS Communication Link: PCM operation is controlled via serial link with DPM.

5.9.2 The PCM Power Converter Circuits

Table 5 and Table 6 present both the secondary voltages generated and their corresponding technical details, while this section delineates the generation process of all requisite secondary voltages for instrument operation. This procedural aspect is accomplished through the coordinated functioning of two DC/DC converters, clarified in the ensuing discussion.

These converters use a multi-output flyback topology with peak current mode control and regenerative clamp which allows the recovery of the energy in the transformer primary winding leakage inductance thus increasing the overall converter efficiency. The design of the converters also incorporates a soft-start circuits that eliminate over-shoots in input current and output voltages when the converter is first powered. Likewise, protections are en-

Table 5 Secondary voltages and DC/DC converters

Voltage, V	DC/DC converter	Module/Unit	Voltage Regulation
+7.0	auxiliary	AEM	cross-regulated
−7.0	auxiliary	AEM	cross-regulated
+3.35	primary	DPM/PSM-MCM	post-regulated
+12	primary	RFM	cross-regulated
±12	primary	PCM analog circuits	cross-regulated

Table 6 Voltages generated by the PCM

Voltage, V	max./min. Voltage, V	Protection, V	Max Ripple p-p, mV	*I* min. Load, mA	*I* max. Load, mA	Including Design Margin, mA
+7.0	+8.0 −6.80	9.00	40	330	1600	1085
−7.0	−6.80 −8.00	−9.00	40	20	100	400
+3.35	+3.40 +3.28	3.75	20	1000	4000	3200
+12.0	+14.00 +12.00	15	75	80	150	

visaged on the Primary and the Auxiliary DC/DC converters. Two important remarks need to be considered at this topic:

- DC/DC converter protections do not contain any active control loop which could interfere with the LCL operation.
- Protection functions are complemented by secondary side protections and handled at FPGA level. Thus, the PCM Primary DC/DC converter includes the following protections on primary side:
  - Input bus under-voltage
  - DC/DC converter over-voltage, over-current, and under-voltage.

If any of the above protections is triggered, the primary DC/DC converter is switched off and the hiccup circuits maintain its state for a minimum period of 100 ms, allowing all DC/DC converter outputs to be reduced to zero. After the programmed delay has elapsed, the DC/DC converter performs a restart attempt. It is important to note that the protection and hiccup circuits include single event protection to avoid false triggering of the protection circuits by a radiation hit. In addition to the converter protections, the GALA PCM FPGA is also capable to provoke a DC/DC converter re-start via an isolated digital interface. The GALA PCM Auxiliary DC/DC converter includes the following protections on primary side:

- DC/DC converter over-voltage and over-current.

If any of the above protections are tripped, the auxiliary DC/DC converter is automatically switched off (without the FPGA intervention). The design of the auxiliary DC/DC converter includes a status signal that is sent to the FPGA, allowing the status of the auxiliary converter to be reported over the communication link. When an auxiliary converter protection trips on the primary side, the FPGA switches the auxiliary converter OFF to prevent the converter from self-starting. The auxiliary converter can be restarted after a protection trip via

remote command. As with the primary DC/DC converter, the protection and hiccup circuits on the auxiliary converter include single-event protection to avoid false triggering of the protection circuits by a radiation hit. The Auxiliary DC/DC converter design includes also a common mode filter on its outputs. Finally, to prevent overvoltage and/or overcurrent that could damage other electronics or modules/units connected to the PCM outputs, the PCM also monitors the voltage and current supplied to the external units. Linear post-regulators are used on DC/DC converter outputs requiring high output voltage accuracy and/or low voltage ripple. All linear regulators included in the GALA PCM design are custom designed in order to achieve ultra-low drop-out at maximum load current in order not to penalize the overall power supply efficiency. The purpose of this post-regulation for the 3.35 V is to ensure that the output voltage remains stable under varying load conditions, temperature changes and other factors. The GALA PCM has in-built capabilities to report to the DPM information on each secondary voltage produced in the converter sensing the value of each voltage, current and the temperature of the PCB.

5.9.3 The PCM Control Circuits

The control circuits are built around an FPGA and are devoted to the control of the operation of the power converter and the collection of its telemetry data. The green area of functional block diagram in Fig. 15 shows this sub-block, where the three main elements of the module can be identified:

i. the digital circuit (FPGA)
ii. the line drivers, and
iii. the analogue conversion circuits.

The core of the module digital circuit is the RTSX32SU-CQ208, an antifuse and radiation tolerant FPGA from Microsemi. This FPGA is specifically designed for enhanced radiation performance in space-based applications. The RTAX-S family has several improvements such as SEU-hardened flip-flops, wider clock lines and stronger clock drivers. SEU-hardened flip-flops are implemented without any user intervention, and offer the benefits of user-implemented triple module redundancy (TMR) without the associated overhead. The PCM layout is shown in Fig. 16.

6 Integration, Verification and Testing

6.1 GALA Verification Tests

The GALA project followed a proto-flight model approach. This had some implications for the qualification strategy of the instrument to identify potential issues early in the program. E.g., the so-called structural-thermal model (STM) was thermally and mechanically representative to the proto-flight (PFM) model. All mechanical parts were identical to the PFM design at preliminary design review (PDR). It was furthermore equipped with highly accurate opto-mechanical mirrors on the base plate, the housing of the unit, at the position of the transmitter folding mirror and the topside of the secondary mirror of the telescope —representing Tx and Rx optical axes— to verify the (co-)alignment and stability of the optical axes before and after vibration and shock testing and throughout the thermal-vacuum cycling test. As the STM did neither include optical lenses or filters, nor electronics components a shock test was performed on a dedicated representative bipod structure for the

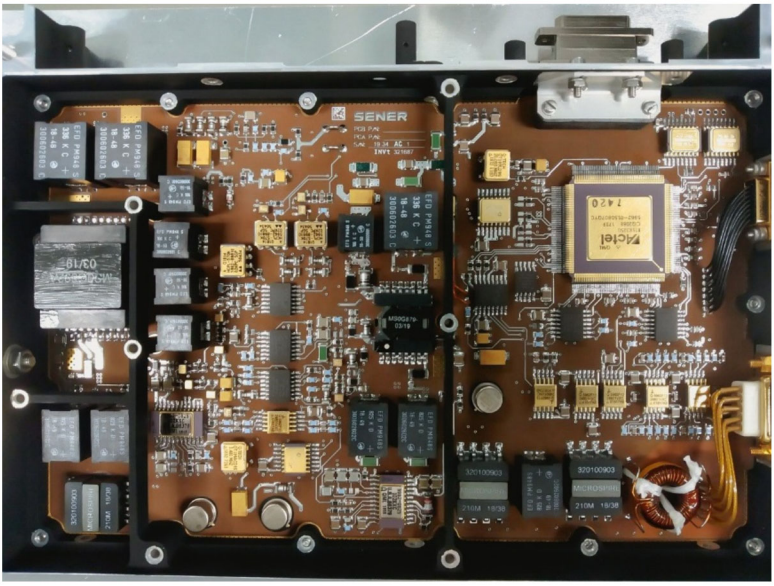

Fig. 16 Power Converter Module (PCM) top view

critical components as the transmitter optical bench assembly, the energy monitor, the Pockels cell driver, the transmitter window and the C-ring sealing. The electronics units LEU and ELU were tested on EM and EQM level, respectively.

The electrical model (EM) was built up with a working flight-like encapsulated laser and a flight-like APD as detector with analogue electronics module. This was particularly important for EMC testing (emission and susceptibility) and evaluation of the performance. The typical expected signals are on the order of 300 photons within some 10 ns. Expressed in frequency domain, this corresponds to a current spectral density of about 330 fA $\mathrm{Hz}^{-\frac{1}{2}}$. Typical noise levels at the spacecraft environment are a few 100 fA $\mathrm{Hz}^{-\frac{1}{2}}$. It is challenging to keep the APD detector free of electronic distortion, the needed noise suppression ratio is more than 100 dB. But also achieving suppression of the noise generated by the powerful laser transmitter electronics inside GALA is necessary, e.g. from pump currents of 200 A within 50 µs, high frequency pulse width modulators or fast switching high voltages of 3 kV for triggering the Pockels cell.

Irradiation testing of optical and electrical components, e.g. exposing them with electron fluxes of up to 8.9×10^{12} at 15 MeV, was done on element level or breadboard level to qualify them for the harsh Jovian environment dominated by electrons.

Finally the PFM units of GALA as well as the complete PFM instrument as system underwent intensive qualification testing. This included again EMC testing, vibration, thermal cycling and balance, alignment and stability testing. These tests were performed under constant monitoring of performance and functionality.

The thermal vacuum test on instrument level was split into two phases; firstly, the electronic units LEU and ELU being inside the vacuum chamber; secondly, the TRU being inside the vacuum chamber. The latter test included also a part of thermal balance testing, where a deep-space simulator, cooled down to −197 °C was set up in front of the TRU's aperture cooling down the telescope to cold non-operational temperatures and testing the

Table 7 Max. and min. temperatures reached during thermal vacuum cycling testing at the transceiver unit TRU. The cold finger interface is attached to the bottom of the TRU dumping the heat generated by the laser and the receiver electronics. (Op. and Nop. mean operational and non-operational)

Interface	Max. Op. temperature	Min. Op. temperature	Max. Nop. temperature	Min. Nop. temperature
cold finger	+41 °C	−7 °C	+50 °C	−37 °C
conductive plate	+10 °C	−46 °C	+36 °C	−51 °C
radiative shroud	+24 °C	−50 °C	+37 °C	−51 °C

survival heaters' performances. This simulator blocked the optical window of the TV chamber. Hence, only laser internal metrology is used to verify performance. The thermal cycling temperatures for the different interfaces obtained during testing are shown in Table 7. During these tests, which were performed in a TV chamber with access to a large aperture 4 m-collimator to perform alignment and pointing stability measurements as well as performance measurements. This setup also allowed feeding in a synthetic optical return pulse into the TRU telescope for testing and verification of the instrument under all relevant thermal conditions. Parts of these tests were also used as reference for the end-to-end test at spacecraft level (see also Sect. 6.4).

6.2 Transmitter

The transmitter laser was tested for the relevant parameters to stay in tight tolerances during the defined environmental conditions. These parameters included amongst others pulse energy, divergence and beam quality, wavelength, and alignment pointing stability. In fact, ensuring the required pointing stability under variation of the environmental and internal temperature was one of the main objectives of the design and was tested intensively. The measured values are listed in Table 8 and Table 9.

6.3 Receiver

The receiver consists of the telescope with backend optics (BEO) and focal plane assembly (FPA). Attached to the focal plane assembly is the analogue electronics module (AEM).

The part BEO/FPA/AEM was tested for function and performance requirements after integration with the GALA PFM optical bench telescope assembly before integration into the GALA TRU PFM instrument. This was done in the 4 m-collimator setup. Several functional and performance test followed. The latter had in particular also the goal to test the scientific performance with nine representative optical pulse shapes fed into the telescope.

6.4 GALA End-to-End Test on the Spacecraft

A spacecraft level verification test is mandatory to verify interfaces and commanding and proper functionality of the instrument after integration on the spacecraft and environmental tests. It is also the goal to exclude any damage of the instrument that might occur during the integration of GALA on the spacecraft. Furthermore, it is necessary to make a minimum special performance test to verify the health of the instrument. For the test, called end-to-end test hereafter, the instrument must be operated including laser firing. Therefore, optical ground support equipment (OGSE) is placed in front of the Transceiver Unit's (TRU) aper-

Table 8 Required and measured main and redundant transmitter laser parameters which were recorded before/during/after environmental testing. M^2 is the beam quality factor; FWHM: Full Width Half Maximum; HV: High Voltage

Parameter	Requirement	Measurement min. Op./ max. Op. temperature	Comment
pulse energy main laser	$\geq$ 17 mJ	18.2...18.3 mJ /18.2...18.5 mJ	at 30 Hz
pulse energy main laser σ	$\leq$ 5%	2.3% /2.0%	at 30 Hz
energy monitor accuracy main laser	$\leq$ 5%	0.8% /1.5%	at 30 Hz
pulse energy red. laser	$\geq$ 17 mJ	17.7...18.0 mJ /18.0...18.1 mJ	at 30 Hz
pulse energy red. laser σ	$\leq$ 5%	1.8% /1.8%	at 30 Hz
energy monitor accuracy red. laser	$\leq$ 5%	2.0% /1.0%	at 30 Hz
divergence main laser	90...110 µrad	107...112 µrad/95...99 µrad	
M^2 main laser	$\leq$ 2.3	2.2 /2.0	
divergence red. laser	90...110 µrad	102...113 µrad/124 µrad	
M^2 red. laser	$\leq$ 2.3	2.3 / 2.5	
pulse duration main laser	5.5 $\pm$ 2.5 ns	4.1...6.6 ns /4.7...6.3 ns	FWHM
pulse duration main laser σ	$\leq$ 500 ps	4.6 ps /2.7 ps	
pulse duration red. laser	5.5 $\pm$ 2.5 ns	3.8...5.5 ns /4.6...6.1 ns	FWHM
pulse duration red. laser σ	$\leq$ 500 ps	7.0 ps /12.4 ps	
wavelength main laser	1064.53 $\pm$ 0.25 nm	1064.39 nm /1064.66 nm	
wavelength red. laser	1064.53 $\pm$ 0.25 nm	1064.38 nm /1064.64 nm	
start pulse amplitude main laser	$\geq$ 0.34 V	0.62 V /0.55 V	HV 350 V, low Gain
start pulse amplitude red. laser	$\geq$ 0.34 V	0.60 V /0.54 V	HV 350 V, low Gain

Table 9 Receiver and transmitter parameters relevant for alignment as measured in the test campaigns

Parameter	Radial [µrad]
nominal RX Field of View (FoV)	282.75
Astigmatism & FoV correction	57.5
effective RX FoV	225.25
main TX beam divergence	56
red. TX beam divergence	62

tures which are to record measurement data, send artificial receiver pulses and dump the laser energy safely. This OGSE is shown in Figs. 17 and 20 as positioned in front of the spacecraft. After GALA has been installed on the JUICE spacecraft the GALA sensor noise data have been carefully analysed for the rare times that GALA had been operated. Although the noise levels were found to be much lower than during the instrument level tests, where the source of the distortions was most likely the laboratory environment and the distortion was picked up by GALA, we could still identify non-random noise, which is assumed to be related to the spacecraft environment.

This shows that despite of all taken design precautions, already small environmental distortions can have an effect on the GALA science performance. A careful characterisation

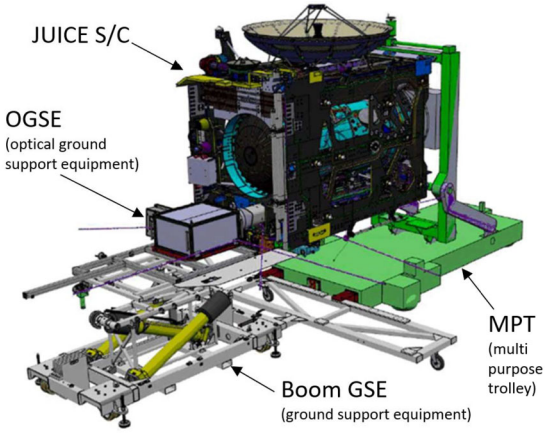

Fig. 17 GALA end-to-end test setup with Optical Ground Support Equipment (OGSE) in front of the Transceiver Unit (TRU) integrated into the JUICE spacecraft

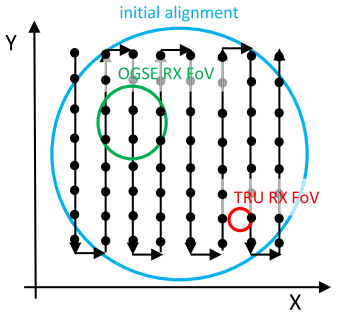

Fig. 18 Scanning scheme for finding the GALA Instrument Line-of-Sight (ILS)

of the GALA science performance in the final spacecraft environment is therefore absolutely mandatory also to allow for tuning the tracking algorithm, that places the range gate at its correct position in time, to suppress specific distortion effects.

The performed end-to-end test with the OGSE is unique among all GALA tests at spacecraft level because it is the only test where representative return signals are detected by GALA. It is the only chance to verify successful tracking of weak return signals from a planetary surface in the spacecraft environment. Therefore, it was considered mandatory by GALA as an end-to-end performance test in the JUICE spacecraft environment.

To perform the GALA end-to-end test, with the aim to verify and to re-measure the GALA performance parameters after spacecraft mechanical testing, it was necessary to have the OGSE placed in front of the TRU and roughly aligned with the GALA instrument line of sight (ILS) (Rx LoS) (Fig. 17). A detailed alignment and stability budget was established to derive respective requirements. With theodolites the misalignment between OGSE (optical cube) and spacecraft reference cube was measured and checked against the OGSE alignment requirements, i.e. 4350 μrad for rotation and 1.8 mm laterally. This was done by mechanically adjusting a special mechanical ground support equipment provided by the satellite prime. The required fine alignment of the OGSE optical Rx path with regard to GALA ILS (TRU Rx LoS) and the narrow field of view of only about 560 μrad was performed with the OGSE internal scan mechanism applying a pattern based scanning scheme (Fig. 18). This worked blindly without having real time access to the data from the GALA instruments. The primary aim was to have the OGSE RX laser, which is generating the return pulse for

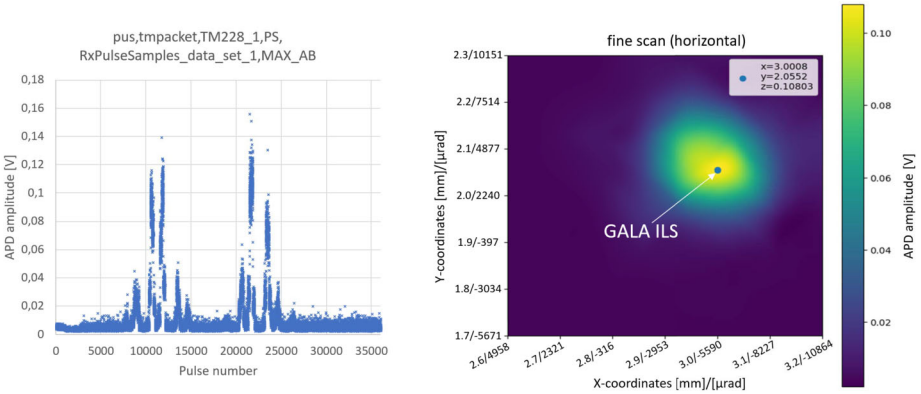

Fig. 19 left: Acquired amplitude for the shots during line-of-sight scan. Each data point represents the detected maximum peak in the range window. Right: Transformed time series into a spatial representation of the GALA ILS. Green and yellow colors show position of detected pulses during line-of-sight scan

Table 10 The tested representative return pulse shapes used during the performance testing of GALA and also during end-to-end test. All pulses are Gaussian shaped

RX pulse name	Energy, fJ	Photons	FWHM, ns
Strong narrow	0.558	2940	13.7
Strong	1.360	7160	31.0
Strong wide	2.182	11,480	47.6
Nominal narrow	0.134	710	13.7
Nominal	0.327	1720	31.7
Nominal wide	0.518	2730	48.7
Weak narrow	0.054	280	11.4
Weak	0.131	690	26.2
Weak wide	0.207	1090	38.8
Super weak narrow	0.027	140	11.4

the GALA RX, aligned with the TRU RX LoS such that the measurement of the GALA performance parameters could be done. The achieved long term stability of the setup was better than 360 µrad and 0.8 mm with micro-vibrations accounting to less than 450 µrad and 0.1 mm (see also Fig. 19).

The test sequence for the end-to-end test was as follows: After a line of sight scan (LoS scan) three blocks were run through. Each of the blocks contained a phase of firing nine different pulse shapes for 5000 pulses for checking of range tracking performance of GALA followed by 50 pulses which were recorded in detail to check time of flight measurements accurately to nanosecond level and with 0.8 ns time resolution. Each phase was separated by a certain strong pulse firing, which was used for synchronization between OGSE and GALA.

The different tested return pulse shapes are simulating the expected return signal based on the assumptions for orbit, albedo and roughness and slope of the planetary surface. The describing parameters for the pulses are listed in Table 10.

As a side effect of the end-to-end test, the GALA ILS measured during spacecraft alignment campaign was verified using the result from TRU RX LoS (GALA ILS) scan and the theodolite measurement result of the OGSE optical cube with regard to the spacecraft ref-

Table 11 The difference between the two measurements is within the measurement accuracy of 510 µrad (half cone). It needs to be highlighted here, that the scan parameters have been optimised such, that the Rx LoS could be found by the OGSE considering all worst-case tolerances of the setup, of course with the drawback of a reduced accuracy

RX LoS Scan in SCRF	RX, µrad	RY, µrad
(converted from OGSE reference frame)	−60	−1259
RX LoS in SCRF	RX, µrad	RY, µrad
(measured in spacecraft alignment campaign via optical cube)	147	−867
residual error	RX, µrad	RY, µrad
difference	−207	−392

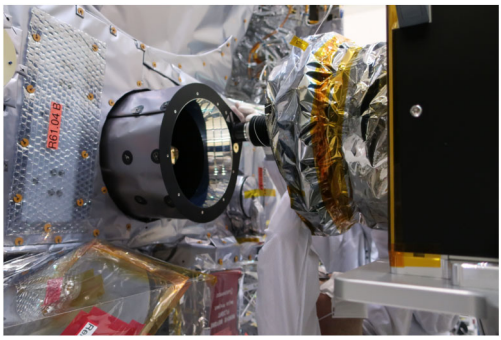

Fig. 20 Optical Ground Support Equipment (OGSE) generating laser return pulses in front of the GALA Transceiver Unit (TRU) mounted on the spacecraft

erence cube. With the knowledge of these alignments (see Table 11) the absolute GALA ILS alignment could be verified to an uncertainty of 510 µrad. Therefore it is shown that a direct line of sight determination of an optical instrument is possible. The uncertainty can be decreased by a finer scanning scheme (Fig. 18) which was not possible due to time schedule constraints in this case.

6.5 Near-Earth Commissioning Phase

Shortly after launch the GALA Near-Earth Commissioning Phase (NECP) took place in May 2023. The full functionality of the instrument, including the transmitter and receiver parts as well as the instrument's electronics and power supply, was tested and the commissioning of the instrument was completed successfully. House-keeping data (temperatures, currents and power) of all units were nominal and no issues either with respect to the hardware nor to the software were observed. The outgoing laser shots were transferred via the fiber optics to the detector and after digitization sampled by the range finder module. The peaks and shapes of the pulses as well as the noise levels at the detector were as expected. Since the commissioning took place in interplanetary space, no return signal could be detected. If the spacecraft constraints allow for operations during the close Moon flyby in August 2024 with a minimum altitude of 700 km, a full return signal from the lunar surface could be detected. With such a measurement, i.e. a GALA ground-track at the lunar surface for several minutes, the full performance of the instrument including the accuracy of the range measurements could be verified.

7 Instrument Performance

The performance model for GALA is adopted from the BepiColombo Laser Altimeter (BELA) which follow the same signal detection method (Gunderson and Thomas 2008, 2010). The performance of GALA is mostly driven by the power of the return pulse.

First, we compute the number of outgoing (Tx) photons n_{Tx} – emitted by the laser – towards the surface. This can be derived from the Tx pulse energy E_{Tx} and the laser wavelength λ_{Tx} by

$$n_{\mathrm{Tx}} = \frac{E_{\mathrm{Tx}}\lambda_{\mathrm{Tx}}}{hc}\,, \tag{2}$$

where h is the Planck constant and c the speed of light in vacuum. The pulse energy is varying with the pulse repetition rate (see Table 4) and gives 9.1×10^{16} and 4.3×10^{16} photons per pulse for 30 Hz and 48 Hz, respectively. The number of reflected photons reaching the GALA APD n_{Rx} is obtained from

$$n_{\mathrm{Rx}} = n_{\mathrm{Tx}}\rho_0\Omega_{\mathrm{TL}}\varepsilon_{Rx}\,, \tag{3}$$

where ρ_0 is the bidirectional reflectance of the surface at zero phase angle, Ω_{TL} the solid angle of the receiver telescope and ε_{Rx} the optical efficiency of the receiver. We assume a Lambertian reflectance of the surface and obtain

$$\rho_0 = \frac{\alpha_{\mathrm{N}}}{\pi}, \tag{4}$$

with the normal albedo α_{N}. The solid angle of the receiver telescope Ω_{TL} is obtained from

$$\Omega_{\mathrm{TL}} = 4\pi\,\sin^2\left(\frac{\theta_{\mathrm{TL}}}{2}\right), \tag{5}$$

with the telescope aperture as seen from the surface θ_{TL}. Given the range to the surface r and the radius of the receiver telescope r_{TL} the telescope aperture is obtained from

$$\theta_{\mathrm{TL}} = \arctan\left(\frac{r}{r_{\mathrm{TL}}}\right). \tag{6}$$

In Table 12 we note the number of received photons for two different ranges and the mean surface albedo of the moons. The optical peak power of the return signal is given by

$$P_{\mathrm{APD}} = \frac{E_{\mathrm{Rx}}}{\sqrt{2\pi}\sigma_{\mathrm{Rx}}} = \frac{n_{\mathrm{Rx}}}{\sqrt{2\pi}\sigma_{\mathrm{Rx}}}\frac{hc}{\lambda_{\mathrm{Tx}}}\,, \tag{7}$$

where E_{Rx} and σ_{Rx} are the energy and temporal pulse width of the return pulse, respectively. The optical power of the pulse is converted by the APD to a photo current which is then converted to a signal voltage by the trans-impedance amplifier. We can express the signal voltage amplitude S by

$$S = P_{\mathrm{APD}}G_{\mathrm{APD}}G_{\mathrm{AEM}}, \tag{8}$$

with G_{APD} being the conversion gain and G_{AEM} the gain of the analogue signal amplifier within the AEM. While G_{AEM} is fixed to two values (low and high), the G_{APD} can be tuned by commanding a different APD bias voltage or temperature.

Table 12 Number of photons reaching the GALA APD in different observational settings. α_N is the normal albedo

Range	Pulse repetition rate	Europa ($\alpha_N = 0.612$)	Ganymede ($\alpha_N = 0.456$)	Callisto ($\alpha_N = 0.186$)
500 km	30 Hz	2577	1920	783
	48 Hz	1213	903	368
1000 km	30 Hz	644	480	195
	48 Hz	303	225	92

The GALA receiver features a very low noise level of only 1.1 mV (the quantization noise of the ADCs is at 0.24 mV). These numbers refer to RMS σ_{DN} of the digitized dark noise within GALA's range window. For the return pulse, we can express the signal-to-noise ratio as

$$SNR = \frac{S}{\sigma_{\mathrm{DN}}}. \tag{9}$$

The SNR is driven by observation conditions, namely the range from the instrument to the surface, surface albedo, surface slope relative to the incoming laser beam, and surface roughness on footprint scale. While the range and albedo affect the energy of the return pulse, the surface slope and roughness modify the temporal pulse width. Hence, when keeping the energy of the return pulse constant, i.e. same range and albedo, the SNR can still decrease due to temporal broadening of the return pulse caused by surface slope and roughness.

In order to assess the performance of GALA, we assume that operations are performed from nadir and we combine the effect of surface slope and roughness to an effective slope value. In Fig. 21 we show GALA's SNR for Europa (top), Ganymede (middle) and Callisto (bottom) in 30 (left) and 48 Hz (right) operation mode as a function of range and return pulse width. Even at Callisto with its low surface albedo, the SNR is greater than one for very narrow return pulses until GALA's maximum ranging distance of 3200 km for operations at 30 Hz. However, the SNR decreases dramatically with higher pulse width. At GALA's minimum ranging distance of 100 km the SNR is above 10 for all three targets and for both operation modes. Typically GALA can start detecting return pulses when the SNR > 1 (dashed white line in Fig. 21). However, the probability of false detections would be rather high. Almost continuous successful detection of return pulses is expected for ranges below 1600 km for Europa, 1400 km for Ganymede and 1100 km for Callisto.

8 Calibration

8.1 On-Ground Calibration

8.1.1 Pointing Stability and Co-Alignment on the Spacecraft

During the TRU alignment campaign it was observed that the TRU folding mirror plays a key role in the Tx alignment and already small thermal gradients have a big impact on the Tx alignment. The movement of the Tx folding mirror during warm up due to laser

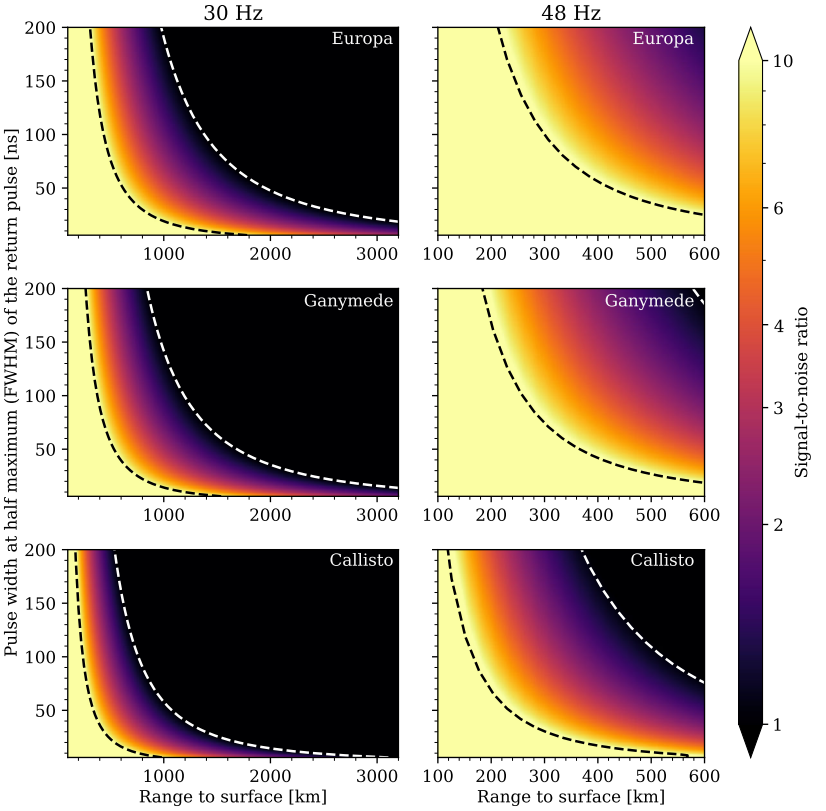

Fig. 21 Signal-to-noise ratio (SNR) for GALA at Europa (top), Ganymede (middle) and Callisto (bottom). The left and right panes provide the SNR for operations in 30 Hz and 48 Hz, respectively. The black dashed line shows SNR values of 10 and the dashed white line an SNR of 1

firing is an effect which will be seen every time the instrument is switched from IDLE to "Laser Firing" mode and accounts for about 60 µrad. The movement of the Tx after start of laser firing is an elastic and reproducible behavior. The effect can be mitigated by switching on the laser 85 min before the actual measurement track starts. As the folding mirror is in the light path of the main and redundant laser both are affected by this folding mirror movement in the same way. Further, as a precaution it was decided not to use the anticontamination heater attached to the folding mirror to prevent permanent misalignments during flight.

The effect of Tx line of sight movement (after warm up of the TRU) has also been characterised. It is shown depending on the cold finger monitoring plate (CFMP) temperature at the TRU in Fig. 22. The four equations give the possibility to correct the Tx position depending on the TRU CFMP temperature by post processing. After spacecraft thermal vacuum balance test the temperature limit of +8 °C and +23 °C have been predicted for the TRU CFMP during the mission. This fact, that the predicted temperature range on spacecraft is much smaller than the qualification temperature range, implies that the movement of the Tx will be small as well.

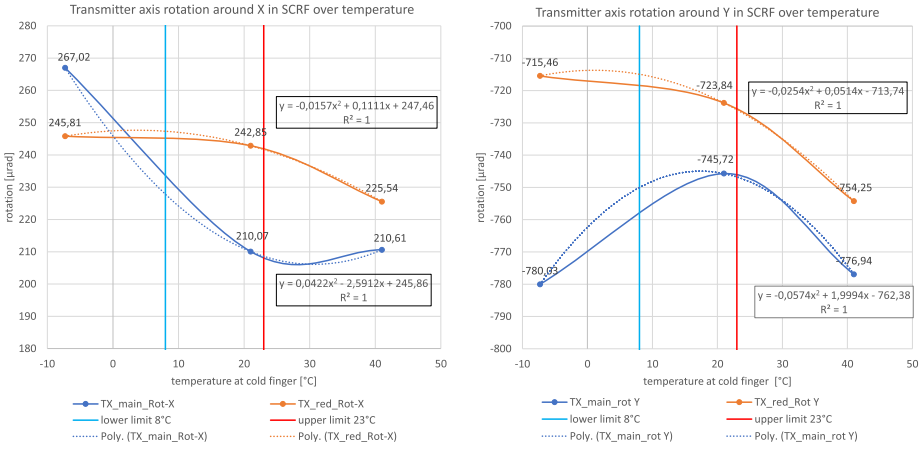

Fig. 22 Transmitter axis rotation around X (left) and Y (right) in spacecraft reference frame (SCRF) over temperature

8.2 In-Flight Calibration

Although the transmitter alignment with respect to the spacecraft was measured on ground, launch effects, e.g., settling, moisture and gravity release, will change the alignment and demand a calibration after launch. In order to determine the exact alignment of the GALA transmitter to the reference frame of the spacecraft, calibration campaigns in cruise and in orbit at Ganymede are considered.

8.2.1 Calibration in Cruise

For the in-cruise transmitter alignment calibration, a down-link from GALA to Laser receiving ground-stations on Earth is considered. A significant driver for the feasibility of the calibration are the constraints on spacecraft attitude applicable during cruise for thermal reasons. For distances to the Sun < 1.3 AU, the high-gain antenna has to be pointed to the Sun using it as a thermal shield. Between 0.98 AU and 1.3 AU off-pointing from that configuration of up to one hour is feasible, and for >1.3 there are no further constraints on the pointing. Thus, beyond 1.3 AU, the spacecraft can be oriented such that the nadir platform points to Earth for the duration of a laser ranging campaign. However, with increasing distance to the Sun the angular separation of Earth and Sun decreases. Here a minimum separation angle of 20° was assumed. This constraint basically limits possible laser ranging campaigns to distances JUICE-Sun below 2.7 AU. Laser ranging at distances larger than 2 AU, however, is subject to the equipment used at the ground station. With the present equipment at a typical ground station, e.g., at the Laser Ranging Station in Wettzell, South of Germany, the calibration residual would be around 4 to 5 arc seconds at a distance of 2 AU from Earth.

During a laser ranging campaign the orientation of JUICE has to be varied in a predefined scheme (scanning window). Possible scan patterns are, e.g., a rectangular scanning pattern or a vortex scanning pattern. Assuming an alignment distortion of GALA due to settling of the optical bench and the GALA transmitter of 140 and 16.5 arc seconds, respectively, the scan window needs to be ± 333 arc seconds (including margin). The slew rate during the

scan is a function of the size of the scan window and the duration of the campaign. For a scan window of ±333 arc seconds and a typical campaign duration of four hours the slew rate is 0.0084 deg/s.

We consider threshold detection for pulse detection at the ground station. The threshold needs to be adjusted against the expected pulse strength and the noise level of the ground station equipment. With increasing distance the number of detected pulses will decline and depending on the noise level and the resulting threshold setting limit the maximum laser ranging distance with current detection capabilities of ground-stations to about 2 AU.

In order to assess the calibration accuracy we performed (Monte Carlo) simulations of laser ranging campaigns with selected Earth-based ground stations. The simulations included errors in the absolute attitude control knowledge and absolute guidance knowledge. For the simulations of measurements at the ground station we considered the link budget of GALA and the performance of ground station equipment. It was found that the calibration residual is below 4 arc seconds for all possible campaigns. The resulting GALA absolute knowledge control error σ_{ACKE} is

$$\sigma_{ACKE} = \sigma_{\phi} + \sigma_{\alpha,\beta} = 11.14" + 4" = 15.14", \tag{10}$$

where $\sigma_{\phi} = 11.14"$ is the knowledge control error without calibration residual (due to harmonic and random GALA and spacecraft attitude errors) and $\sigma_{\alpha,\beta} = 4"$ is the calibration residual. The obtained value of 15.14" is satisfying the requirement for the GALA pointing knowledge.

8.2.2 Calibration at Ganymede

Three calibration approaches are considered in orbit at Ganymede. The first approach makes use of GALA's accurate range measurement capability. By changing the geometry of the measurement, i.e. introducing an off-nadir angle, we can translate the positioning error, resulting from an alignment knowledge error, into a height error. Through comparison of a nadir and off-nadir observations we can calibrate the GALA Tx alignment. With this method, the resulting absolute knowledge control error σ_{ACKE} is about 20" for an off-nadir angle of 20°.

The other two approaches involve the science observations provided by the camera JANUS. First, by compiling a digital terrain model (DTM) from stereo images acquired simultaneously with a GALA profile, a cross-calibration of the two instruments can be performed through co-registration of the topographic data sets. Estimated residuals σ_{ACKE} would be around 20". The second calibration approach is a direct detection of the GALA return laser pulse by JANUS using long exposures (several seconds) on the night-side of Ganymede. If the signal-to noise ratio of the spot is sufficiently high in stacked images, the pixels where the GALA return pulse hits the JANUS detector could be identified. This can then be easily referred to the spacecraft reference frame by JANUS star calibrations. The accuracy of this method would be limited by the field of view of one pixel (15 μrad for JANUS) and the accuracy of the CCD alignment against the spacecraft inertial frame which is expected to be of the order of a few arc seconds.

Apart from the transmitter pointing knowledge the receiver noise levels have to be calibrated. It is exposed to the hard radiation environment at Jupiter, and thus it is expected that the GALA APD will degrade and changing its responsivity and noise level over time. These detector characteristics need to be known to setup the gain profile of GALA and to minimize the probability of false detection in the Ganymede orbit phase. A characteriza-

tion of the degradation can be accomplished by repeated measurements at the same region separated in time. For the on-orbit detector calibration no special spacecraft activities are required. In addition the dark noise of the detector is monitored throughout the cruise phase in regular check-outs.

9 Operational Strategy

GALA's operational concept is simple: Whenever a target body is in its field of view and the distance to the surface is close enough to detect a return pulse, GALA can perform active laser operations. This simple concept is mainly constrained by the trajectory and the pointing of the JUICE spacecraft.

According to the current knowledge from ground-testing and models of the satellite surfaces, GALA will be sensitive to range measurements at altitudes below 1600 km, 1400 km, and 1100 km, at Europa, Ganymede, and Callisto assuming a mean surface slope of 8°. The differing performance of GALA at specific altitudes mainly results from different albedo values of the satellite surfaces at the laser wavelength of 1064 nm. Potential operational phases of GALA, in which the altitude constraint is fulfilled, are listed in Table 13. The ground tracks for which the altitude constraints are fulfilled during the flyby at Callisto and Europa are shown as red curves in Fig. 23.

Operations will typically start and end at 3200 km distance to the surface (blue curves in Fig. 23), which is defined by the technical limit for active ranging operations of GALA. GALA is able to operate at shot frequencies between 1 Hz and 48 Hz with 30 Hz being the nominal frequency. An increase of the shot frequency above 30 Hz is only possible if GALA is closer than approximately 1000 km to the surface. With a higher frequency, the laser shot energy and range window start length have to be reduced. Thus the overall operational altitude decreases. GALA is also very flexible in terms of telemetry. Several predefined data masks allow a direct definition of the "per-shot" data rate upon start of science operations. This in combination with the possible shot frequencies, which are also specified upon start of science operations, allows for a very precise configuration and commanding for specific scientific purposes.

The surface coverage of Ganymede by the GALA instrument is subject to operation time and the spacecraft orbit. Due to the polar orbit of JUICE the coverage is best at polar regions (excluding the very poles above/below ±82°) and limited at equatorial regions with greater cross-track spacing of the ground-tracks. The gaps at the poles and in the equatorial regions, however, could be closed with dedicated off-nadir pointing. Restrictions on the operation time of GALA introduce large gaps in the coverage and significantly decrease the recovered information especially in terms of regional and local topography and surface roughness.

The diameter of the GALA footprints correlates linearly with the altitude and can be estimated by d_{spot} = altitude in m/10,000. In other words, at an altitude of 1000 km, the footprint diameter will be 100 m. The different laser spot sizes and diameters are shown in Fig. 24 for typical operation scenarios.

The best resolution achievable with GALA is limited by the diameter of the GALA footprint of 50 m at 500 km altitude and 20 m at 200 km altitude during the GCO-500 and GCO-200 phases, respectively. However, there are only distinct areas in high-latitude regions where the density of footprints is sufficient to have a continuous coverage at this resolution. In equatorial regions gaps of a few km (exact value depending on total operation time) will remain.

Table 13 Possible operational phases for GALA at Ganymede, Europa, and Callisto. Operational times are based on altitude, i.e. when JUICE is below the critical altitude. CA: Closest Approach, d_{spot} laser spot diameter at CA; S2S: distance from one laser Spot center to the next laser spot center during closest and furthest operational distance at 48 Hz for flybys, elliptical orbit phase (GEO) and GCO-200 and 30 Hz for GCO-500; GEO: Ganymede Elliptical Orbit, GCO: Ganymede Circular Orbit; Table data was generated with the meta-kernel for JUICE Dataset v436 – Planning 20231204-001

Type	Body	Date	Duration $[min]$	CA $[km]$	d_{spot} CA $[m]$	S2S farthest distance $[m]$	S2S closest distance $[m]$
Fly-By	Ganymede	2031-07-21	11	397	40	84	149
Fly-By	Ganymede	2032-02-13	14.48	397	40	65	115
Fly-By	Ganymede	2032-04-11	13.8	485	49	67	113
Fly-By	Europa	2032-07-02	21.45	401	40	26	67
Fly-By	Europa	2032-07-16	21.3	401	40	26	67
Fly-By	Callisto	2032-09-10	14.35	200	20	61	110
Fly-By	Callisto	2032-09-27	14.33	200	20	61	110
Fly-By	Callisto	2032-10-14	14.33	200	20	61	110
Fly-By	Callisto	2032-10-30	14.35	200	20	61	110
Fly-By	Callisto	2032-11-16	14.33	200	20	61	110
Fly-By	Callisto	2033-05-10	13.5	313	31	63	105
Fly-By	Callisto	2033-06-04	14.35	200	20	61	110
Fly-By	Callisto	2033-06-21	14.35	200	20	61	110
Fly-By	Callisto	2033-07-08	14.35	200	20	61	110
Fly-By	Callisto	2033-07-24	14.35	200	20	61	110
Fly-By	Callisto	2033-08-10	14.32	200	20	61	110
Fly-By	Callisto	2033-11-01	13.52	316	32	63	105
Fly-By	Ganymede	2033-11-27	18.33	864	86	48	64
Fly-By	Callisto	2034-02-14	21.13	643	64	39	52
GEO-1 7x close	Ganymede	20.12.2034 - 23.12.2034	40...66	197...1166	20...117	23...24	29...49
GEO-3 38x close	Ganymede	13.05.2035 - 21.05.2035	50...127	520...1114	52...111	21...25	28...34
GCO-500	Ganymede	21.05.2035- End of Mission	>132 days	455	45...55	45	55
GCO-200	Ganymede	extended mission	TBD	200	20	27	33

10 Systematic Data Products

GALA observational data will provide information on distance to the surface from the time of flight of detected laser return pulses, and on surface albedo as well as slopes and roughness through pulse width and energy. Albedo can also be determined from passive intensity measurements, while pulse shape can be recorded also in the form of pulse discrimination parameters and original, time-resolved sensor samples, depending on data rate. GALA raw and calibrated data products to be released through the Planetary Science Archive (PSA) at regular intervals will reflect this variability through the provision of optional supplemental datasets, as described in the following. We also discuss GALA derived data products, which will rely on scientific data processing, analysis of external data, and aggregated GALA datasets. For example, absolute position with respect to a body-fixed coordinate sys-

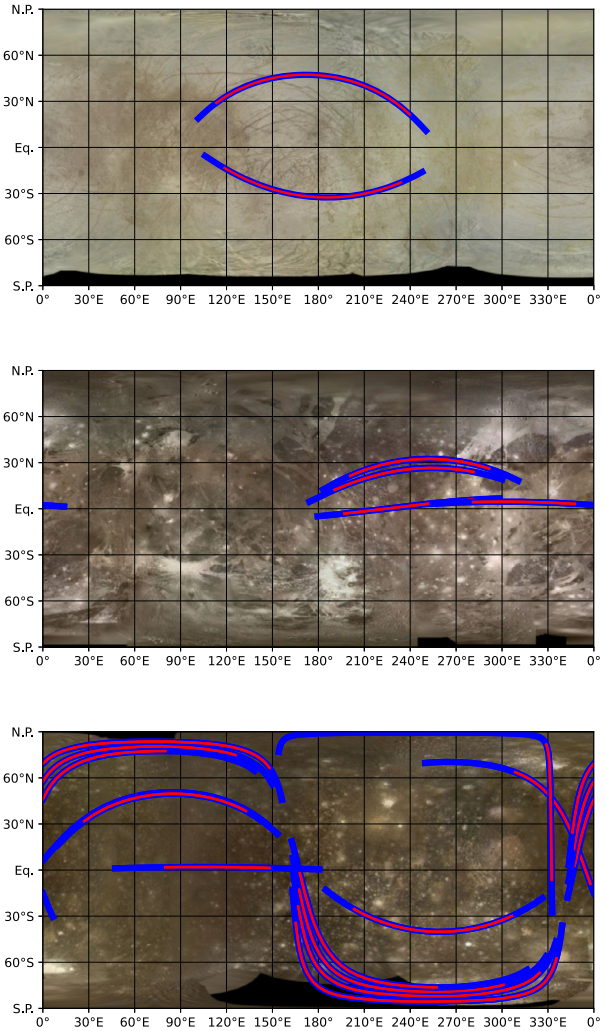

Fig. 23 Laser tracks of GALA of flybys on Europa (top), Ganymede (middle), and Callisto (bottom). Red curves denote altitudes where GALA is expected to receive a stable signal. These altitudes are 1600 km, 1400 km and 1100 km for Europa, Ganymede and Callisto, respectively. The blue curves denote altitudes below 3200 km at which laser ranging will start/stop at the flybys. The presented figures are based on the trajectory scenario CREMA 5.1_150LB_23

tem allows assessment of topographic heights, and studies of the global shape properties and planetary rotational dynamics. GALA topographic profiles will also be used to create digital terrain models that can serve as precise geodetic reference datasets. Topography maps as well as other global maps such as surface roughness maps will also be used for quantitative geological investigation, such as surface morphology, tectonics, volcanism, surface ages, and the evolution of the planet.

GALA, according to the three different regular operation modes of the instrument, provides three basic types of science observation data:

1. In RFM PULSE mode, the pulse discrimination operates on both emitted and received pulse, and a set of pulse detection parameters (centroid position and FWHM) is generated for the emitted pulse and for up to four candidates for received pulse. Thereby, the four candidates comprise the most powerful signals within the range window (RW). The range window is a time interval of 200.8 μs at which the instrument expects the arrival of the

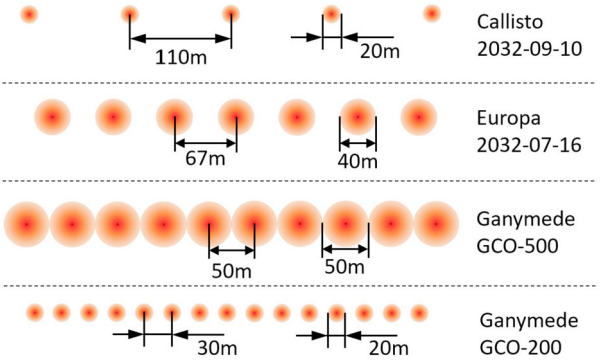

Fig. 24 Scaled laser spot distances and diameters for specific Callisto and Europa flybys during closest approach at 48 Hz shot frequency and for Ganymede during GCO-500 and GCO-200 at 30 Hz and 48 Hz, respectively (see Table 24)

return pulse. Optionally, correlation window (CW) samples (CWS), i.e. sub-sets of the original, time-resolved range window samples (RWS), can be recorded.

2. In RFM SENSOR mode, pulse discrimination operates on the outgoing laser pulse only, while the complete set of range window sample (RWS) values is recorded for the incoming signal.
3. In RFM ALBEDO mode, the instrument passively measures the ambient radiation at the laser wavelength of 1064 nm and records a full set of sensor sample values, for the time equivalent of one range window. The data records in GALA data product files resulting from each of these operation modes are denoted as PULSE data records, SENSOR data records, and ALBEDO data records, respectively.

The selection of data items included in the science telemetry is configurable by software, according to data volume constraints and scientific purpose. The selection is controlled by data masks which can be modified by telecommand, or amended by new ones. The data masks are used to control the telemetry data rate and may e.g. differ by the number of transmitted return pulse candidates. Different data masks will be used dependent on the signal-to-noise ratio, which is mainly driven by the ranging distance. With the usage of different data masks, a large variability in the content of the received data packets from GALA is obtained. In contrast to this, the archived GALA data products are adopting a more uniform and user-friendly set of data structures, which, because of the large potential variability of GALA telemetry content, implies that certain subsets of data items or fields might be unused in a given product file (i.e. contain Null values).

GALA raw data products store the measurement data in a form close to the telemetry data received from the spacecraft, in accordance with the PDS 4 standard. They include all of the GALA telemetry data items needed to produce the next higher product level (Calibrated), subsequently. Units are not converted, no ancillary calibration data and no data resampling is applied. Reformatting of data items to obtain standard data types is applied where telemetry data items are packed into customary bit representations or compound data records to reduce the telemetry data volume.

GALA raw data are stored in binary data tables (called Altimetry Data Records, ADR), each containing data for a specific observation sequence (e.g. a single flyby or one Ganymede orbit). Two types of ancillary binary data tables containing collections of sensor sample data records are provided optionally, depending on the instrument operation mode. Correlation window sample tables (CWS), i.e. 0.525 μs subsets of the range window containing a return pulse candidate, are produced when PULSE or SENSOR data records are included in the telemetry data. Range window sample tables (RWS), containing the complete 200.8 μs range window time interval, are produced when SENSOR or ALBEDO data

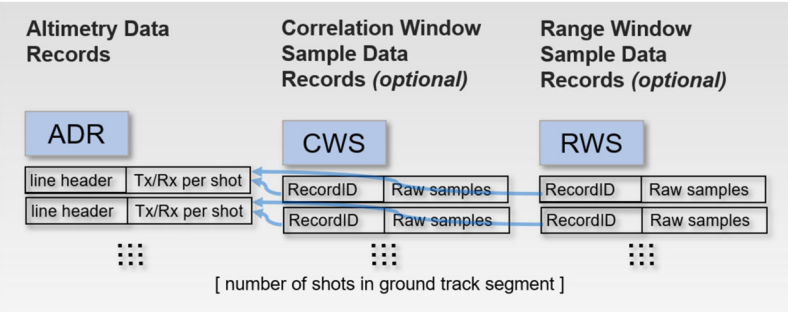

Fig. 25 File organization for GALA Altimetry Data Records (ADR) and optional supplemental data tables, applicable to all science observation modes and for both Raw and Calibrated product data sets

records are included in the telemetry data. The general structure of the three types of data tables is the same for all operation modes (see Fig. 25 for a schematic representation). All tables are fixed-length binary tables and are organized on a *per shot* basis, i.e. data related to one laser shot (or reflectance measurement in ALBEDO mode) are reported on a single row. Each set of sensor sample values in the optional supplemental sample tables is linked to a unique data record (i.e. row) in the ADR data table.

Each row in the Raw ADR tables basically consists of a line header followed by a set of data items recording the observation data for emitted pulse signals (Tx signal) and received signals (Rx signal). In PULSE mode data records, Rx parameters for up to four alternative return pulse candidates can be present. The line header provides identifiers for the type of data record and index numbers showing whether corresponding data records in the CWS and RWS tables are present and, if applicable, their row number. In addition, the line header contains timing and gain parameters for the data record. The rows of CWS and RWS tables consist of a record identifier storing the row index of the respective data record in the ADR table, followed by the sensor sample values.

GALA Calibrated data products store measurement data in number and time stamp formats in accordance with the current PDS 4 standard. Data values are converted to physical units, where applicable. While the general structure of GALA Calibrated data tables is the same as for Raw data tables (Fig. 25), they partly differ in terms of contained data items. The Calibrated product, for example, includes two preliminary ranging parameters in PULSE mode data records: the `NominalTimeOfFlight`, providing the measured time difference in milliseconds between emitted and return pulse, according to the nominal value for the sampling rate, and the `CoarseRange`, providing the measured distance to the surface along the line of sight in kilometers, according to `NominalTimeOfFlight`, and not considering the relative motion between spacecraft and target. As for the Raw product, Rx parameters and ranging parameters for up to four alternative return pulse candidates can be present. GALA Calibrated CWS and RWS tables, if present, contain the sensor samples available also in the corresponding table of the Raw product, now corrected for electronic offsets and normalized according to the gain factor of the analog electronics. GALA derived data products will rely on scientific processing methodology and will require, as input for their production, external observation data (e.g. spacecraft position and attitude)and/or aggregated GALA data sets, the latter consisting of data from multiple orbital passes for a region, or globally. Three categories of GALA Derived products can be distinguished, based on the type and coverage (spatial and temporal) of required input data:

1. Calibrated geo-located altimetry data records (i.e. 3D surface points), and derived height profiles, 3D models, and map products will result from the combination of GALA calibrated data with data on spacecraft position and attitude. This allows converting from inertial to body-fixed co-ordinates and applying two-way light-time correction including the effect of relative motion between spacecraft and body.
2. Results from analysis of an aggregated and, ultimately, global GALA data set. In addition to an increased resolution of regional data products, an example for additional information obtainable from aggregated datasets are profile offsets determined at crossover-points.
3. Results from joint analysis of GALA data with observational data from other scientific instruments.

Derived data products are expected to undergo revision during the course of the mission, as the knowledge on instrument geometry, spacecraft position, spacecraft attitude, and planetary rotational dynamics may evolve, and while additional observational data become available.

11 Summary and Conclusion

GALA will be the first laser altimeter in the outer solar system acquiring range measurements of the icy moons of Jupiter: Ganymede, Europa, and Callisto. It will obtain global, regional and local topography of Ganymede from flybys and especially from JUICE' final 500-km and 200-km orbital phases. In addition, Europa's and Callisto's geology, surface roughness, albedo, and global shapes will be investigated from altimetry ground-tracks during close flybys at altitudes less than 1600 and 1100 km, respectively. From the digitally sampled return pulse GALA will, in addition to the range measurements, determine the surface roughness and slopes at the scale of the laser footprint of about 50 m at an altitude of 500 km (GCO-500) and 20 m at 200 km (GCO-200) altitude, respectively. In addition, it will measure the albedo of the terrain at the laser wavelength of 1064 nm. The instrument's precision for ranging will be on the order of 10 cm as verified by ground-testing of the flight configuration. However, due to uncertainties in spacecraft position and pointing knowledge, the accuracy for topographic data will be on the order of a few meters, which will enable the defined scientific requirements. In addition to global, regional and local topographic data, GALA will measure the radial tidal deformation of Ganymede on the orbital frequency of the satellite. From the determination of the solid-body tidal Love number h_2, possibly including its phase-lag, conclusions on the existence and characteristics of a global subsurface ocean on Ganymede will be drawn. This measurement will be complementary to other instruments characterizing the ocean, in particular 3GM's determination of the tidal potential Love number k_2, and J-MAG's determination of the induced magnetic fields at Ganymede.

Simulation and end-to-end testing on the ground has shown full compliance of the GALA flight-model performance with the mission's science requirements. In-flight testing in the Near-Earth commissioning phase has demonstrated full functionality of the instrument in cruise.

Abbreviations

3GM Gravity and Geophysics of Jupiter and Galilean Moons
ACKE Absolute Knowledge Control Error
ADC Analog-to-Digital Converter
ADR Altimetry Data Records

AEM Analog Electronics Module
APD Avalanche Photo Diode
AU Astronomical Unit
BELA BepiColombo Laser Altimeter
BEO Backend Optics
CA Closest Approach
CCD Charge-Coupled Device
CFMP Cold Finger Monitoring Plate
CMD Command
CSU Collimator Sensor Unit
CWS Correlation Window Samples
DAC Digital-to-Analog Converter
DC/DC Direct Current to Direct Current converter
DCL Declared Component List
DEM/DTM Digital Elevation/Terrain Model
DLR German Aerospace Center
DPM Digital Processing Module
EDAC Eror Detection and Correction
ELU Electronics Unit
EM Electrical Model
EMC Electromagnetic Compatibility
EMI Electromagnetic Interference
EQM Engineering Qualification Model
ESA European Space Agency
ESAC European Space Astronomy Centre
ESATAN-TMS European Space Thermal Analysis Network
ESOC European Space Operations Centre
ESTEC European Space Research and Technology Centre
FASTRAD Radiation Analysis Software
FPA Focal Plane Assembly
FPGA Field Programmable Gate Array
FWHM Full Width at Half Maximum
GALA Ganymede Laser Altimeter
GCO-200 Ganymede Circular Orbit phase at 200 km altitude
GCO-500 Ganymede Circular Orbit phase at 500 km altitude
GCR Galactic Cosmic Rays
GEO Ganymede Elliptical Orbit
GRAS Geant4 Radiation Analysis Software
HK Housekeeping Data
HV High-Voltage Supply
I/F Interface
ILS Instrument Line of Sight
ISO International Organization for Standardization
JANUS Jovis, Amorum ac Natorum Undique Scrutator (JUICE camera)
J-MAG JUICE Magnetometer
JUICE JUpiter ICy moons Explorer
LDO Low Dropout Regulator
LEOP Low Earth Orbit Phase
LET Linear Energy Transfer

LEU Laser Electronics Unit
LHM Laser Head Module
LiDAR Light Detection and Ranging
LOLA Lunar Orbiter Laser Altimeter
LoS Line of Sight
LVDS Low-Voltage Differential Signaling
MAJIS Moons and Jupiter Imaging Spectrometer
MLA Mercury Laser Altimeter
MLI MultiLayer Insulation
MOLA Mars Laser Altimeter
MOSFET Metal–Oxide–Semiconductor Field-Effect Transistor
MRAM Magnetoresistive Random-Access Memory
Msps Mega Samples per Second
NASA National Aeronautics and Space Administration
Nd:YAG Neodymium-doped Yttrium Aluminum Garnet
NECP Near-Earth Commissioning Phase
NEP Noise Equivalent Power
OGSE Optical Ground Support Equipment
PCB Printed Circuit Board
PCDU Power Conditioning and Distribution Unit
PCM Power Converter Module
PDR Preliminary Design Review
PDS Planetary Data System
PFM Proto-Flight Model
POL Point of Load
PPS Pulse Per Second
PROM Programmable Read-Only Memory
PSA Planetary Science Archive
PSM-MCM Power Supply Module
RFM Range Finder Module
RIME Radar for Icy Moon Exploration
RPWI Radio and Plasma Wave Instrument
RWS Range Window Samples
Rx Receiver
S/C Spacecraft
S2S Spot-to-Spot
SCRF Spacecraft Reference Frame
SDRAM Synchronous Dynamic Random-Access Memory
SEB Single Event Burnout
SEDR Single Event Dielectric Rupture
SEE Single Event Effects
SEGR Single Event Gate Rupture
SEL Single Event Latch-up
SESB Single Event Snapback
SEU Single Event Upset
Si-APD Silicon Avalanche Photodiode
SNR Signal-to-Noise Ratio
SPE Solar Particle Events
SpW SpaceWire

SSI Synchronous Serial Interface
STM Structural and Thermal Model
TC Telecommand
TCS Thermal Control System
TIA Transimpedance Amplifier
TID Total Ionizing Dose
TM Telemetry
TMR Triple Modular Redundancy
TNID Total Non-Ionizing Dose
TRP Thermal Reference Point
TRU Transceiver Unit
TV Thermal Vacuum
Tx Transmitter

Acknowledgements We would like to thank two anonymous reviewers for their helpful comments on previous versions of the manuscript. We thank William Byrne for carefully reading and commenting the manuscript. Financial support was provided on behalf of the DLR Space Agency by the Federal Ministry of Economic Affairs and Climate Action of Germany (FKZ: 50QJ 1401). We gratefully acknowledge the support by the JUICE project teams at ESTEC, ESOC, ESAC and Airbus Defence & Space in Friedrichshafen and Toulouse.

A portion of this work was carried out by the Jet Propulsion Laboratory, California Institute of Technology, under a contract with NASA.

Funding Information Open Access funding enabled and organized by Projekt DEAL.

Declarations

Competing Interests The authors declare no competing interests.

References

Aharonson O, Zuber MT, Rothman DH (2001) Statistics of Mars' topography from the Mars orbiter laser altimeter: slopes, correlations, and physical models. J Geophys Res, Planets 106(E10):23723–23736. https://doi.org/10.1029/2000JE001403

Anderson JD, Lau EL, Sjogren WL, Schubert G, Moore WB (1996) Gravitational constraints on the internal structure of Ganymede. Nature 384(6609):541–543. https://doi.org/10.1038/384541a0

Araki H, Tazawa S, Noda H, Ishihara Y, Goossens S, Sasaki S, Kawano N, Kamiya I, Otake H, Oberst J, Shum C (2009) Lunar global shape and polar topography derived from kaguya-LALT laser altimetry. Science 323(5916):897. https://doi.org/10.1126/science.1164146

Archinal BA, Acton CH, A'Hearn MF, Conrad A, Consolmagno GJ, Duxbury T, Hestroffer D, Hilton JL, Kirk RL, Klioner SA, McCarthy D, Meech K, Oberst J, Ping J, Seidelmann PK, Tholen DJ, Thomas PC, Williams IP (2018) Report of the IAU working group on cartographic coordinates and rotational elements: 2015. Celest Mech Dyn Astron 130(3): 22. https://doi.org/10.1007/s10569-017-9805-5

Behounkova M, Tobie G, Choblet G, Cadek O (2012) Tidally-induced melting events as the origin of south-pole activity on Enceladus. Icarus 219(2):655–664. https://doi.org/10.1016/j.icarus.2012.03.024

Bland MT, Showman AP, Tobie G (2009) The orbital-thermal evolution and global expansion of Ganymede. Icarus 200(1):207–221

Boutonnet A, Langevin Y, Erd C (2024) Designing the JUICE trajectory. Space Sci Rev 220:67. https://doi.org/10.1007/s11214-024-01093-y

Cheng AF, Barnouin-Jha O, Zuber MT, Veverka J, Smith DE, Neumann GA, Robinson M, Thomas P, Garvin JB, Murchie S, Chapman C, Prockter L (2001) Laser altimetry of small-scale features on 433 eros from NEAR-shoemaker. Science 292(5516):488–491. https://doi.org/10.1126/science.1058330

Cheng AF, Barnouin-Jha O, Prockter L, Zuber MT, Neumann G, Smith DE, Garvin J, Robinson M, Veverka J, Thomas P (2002) Small-scale topography of 433 eros from laser altimetry and imaging. Icarus 155(1):51–74. https://doi.org/10.1006/icar.2001.6750

Culberg R, Schroeder D, Steinbrügge G (2022) Double ridge formation over shallow water sills on Jupiter's moon Europa. Nat Commun 13:2007

Davies ME, Colvin TR, Oberst J, Zeitler W, Schuster P, Neukum G, McEwen AS, Phillips CB, Thomas PC, Veverka J, Belton MJS, Schubert G (1998) The control networks of the Galilean satellites and implications for global shape. Icarus 135(1):372–376. https://doi.org/10.1006/icar.1998.5982

Dermott SF (1979) Shapes and gravitational moments of satellites and asteroids. Icarus 37(3):575–586. https://doi.org/10.1016/0019-1035(79)90015-0

Dougherty M, et al (2025) Space Sci Rev 221

Enya K, Kobayashi M, Kimura J, Araki H, Namiki N, Noda H, Kashima S, Oshigami S, Ishibashi K, Yamawaki T, Tohara K, Saito Y, Ozaki M, Mizuno T, Kamata S, Matsumoto K, Sasaki S, Kuramoto K, Sato Y, Yokozawa T, Numata T, Mizumoto S, Mizuno H, Nagamine K, Sawamura A, Tanimoto K, Imai H, Nakagawa H, Kirino O, Green D, Fujii M, Iwamura S, Fujishiro N, Matsumoto Y, Lingenauber K, Kallenbach R, Althaus C, Behnke T, Binger J, Daurskikh A, Eisenmenger H, Heer U, Hüttig C, Lara LM, Lichopoj A, Lötzke H-G, Lüdicke F, Michaelis H, Pablo Rodriguez Garcia J, Rösner K, Stark A, Steinbrügge G, Thabaut P, Thomas N, Togno S, Wahl D, Wendler B, Wickhusen K, Willner K, Hussmann H (2021) The Ganymede Laser Altimeter (GALA) for the Jupiter ICy moons Explorer (JUICE): mission, science, and instrumentation of its receiver modules. Adv Space Res. https://doi.org/10.1016/j.asr.2021.11.036

Giese B, Oberst J, Roatsch T, Neukum G, Head JW, Pappalardo RT (1998) The local topography of uruk sulcus and Galileo regio obtained from stereo images. Icarus 135(1):303–316. https://doi.org/10.1006/icar.1998.5967

Giese B, Wagner R, Hussmann H, Neukum G, Perry J, Helfenstein P, Thomas PC (2008) Enceladus: an estimate of heat flux and lithospheric thickness from flexurally supported topography. Geophys Res Lett 35(24):24204. https://doi.org/10.1029/2008GL036149

Golle O, Dumoulin C, Choblet G, Čadek O (2012) Topography and geoid induced by a convecting mantle beneath an elastic lithosphere. Geophys J Int 189(1):55–72. https://doi.org/10.1111/j.1365-246X.2012.05364.x

Golombek MP, Banerdt WB (1986) Early thermal profiles and lithospheric strength of Ganymede from extensional tectonic features. Icarus 68(2):252–265. https://doi.org/10.1016/0019-1035(86)90022-9

Gomez Casajus L, Ermakov AI, Zannoni M, Keane JT, Stevenson D, Buccino DR, Durante D, Parisi M, Park RS, Tortora P, Bolton SJ (2022) Gravity field of Ganymede after the Juno extended mission. Geophys Res Lett 49(24):2022–099475. https://doi.org/10.1029/2022GL099475

Grasset O, Dougherty MK, Coustenis A, Bunce EJ, Erd C, Titov D, Blanc M, Coates A, Drossart P, Fletcher LN, Hussmann H, Jaumann R, Krupp N, Lebreton JP, Prieto-Ballesteros O, Tortora P, Tosi F, Van Hoolst T (2013) JUpiter ICy moons Explorer (JUICE): an ESA mission to orbit Ganymede and to characterise the Jupiter system. Planet Space Sci 78:1–21

Greeley R, Chyba CF, Head JW, McCord TB, McKinnon WB, Pappalardo RT, Figueredo PH (2004) Geology of europa. In: Bagenal F, Dowling TE, McKinnon WB (eds) Jupiter: the planet, satellites and magnetosphere. Cambridge University Press, pp 329–362

Gunderson K, Thomas N (2008) Polarimetric NIR reflectance measurements of regolith simulants at zero phase angle. Planet Space Sci 56(15):1925–1938. https://doi.org/10.1016/j.pss.2008.09.004

Gunderson K, Thomas N (2010) BELA receiver performance modeling over the BepiColombo mission lifetime. Planet Space Sci 58(1–2):309–318. https://doi.org/10.1016/j.pss.2009.08.006

Head J, Pappalardo R, Collins G, Belton MJS, Giese B, Wagner R, Breneman H, Spaun N, Nixon B, Neukum G, Moore J (2002) Evidence for Europa-like tectonic resurfacing styles on Ganymede. Geophys Res Lett 29(24):2151. https://doi.org/10.1029/2002GL015961

Hirata N, Suetsugu R, Ohtsuki K (2020) A global system of furrows on Ganymede indicative of their creation in a single impact event. Icarus 352:113941. https://doi.org/10.1016/j.icarus.2020.113941

Hubbard WB, Anderson JD (1978) Possible flyby measurements of Galilean satellite interior structure. Icarus 33(2):336–341. https://doi.org/10.1016/0019-1035(78)90153-7

Hussmann H, Sohl F, Oberst J (2011) Measuring tidal deformations at Europa's surface. Adv Space Res 48(4):718–724

Hussmann H, Lingenauber K, Kallenbach R, Enya K, Thomas N, Lara LM, Althaus C, Araki H, Behnke T, Castro-Marin JM, Eisenmenger H, Gerber T, Herranz de la Revilla M, Hüttig C, Ishibashi K, Jiménez-Ortega J, Kimura J, Kobayashi M, Lötzke H-G, Lichopoj A, Lüdicke F, Martínez-Navajas I, Michaelis H, Namiki N, Noda H, Oberst J, Oshigami S, Rodríguez García JP, Rodrigo J, Rösner K, Stark A, Steinbrügge G, Thabaut P, del Togno S, Touhara K, Villamil S, Wendler B, Wickhusen K, Willner K (2019) The Ganymede laser altimeter (GALA): key objectives, instrument design, and performance. CEAS Space J 11(4):381–390. https://doi.org/10.1007/s12567-019-00282-8

Hussmann H, Schubert G, Steinbrügge G, Sohl F, Kimura J (2023) Internal structure of Ganymede. In: Volwerk M (ed) Ganymede. Cambridge University Press, pp 77–86

Iess L, et al (2025) Space Sci Rev 221

Jones KB, Head JW, Pappalardo RT, Moore JM (2003) Morphology and origin of palimpsests on Ganymede based on Galileo observations. Icarus 164(1):197–212. https://doi.org/10.1016/S0019-1035(03)00128-3

Kamata S, Kimura J, Matsumoto K, Nimmo F, Kuramoto K, Namiki N (2016) Tidal deformation of Ganymede: sensitivity of love numbers on the interior structure. J Geophys Res, Planets. https://doi.org/10.1002/2016je005071

Kimura J, Hussmann H, Kamata S, Matsumoto K, Oberst J, Steinbrugge G, Stark A, Gwinner K, Oshigami S, Namiki N, Lingenauber K, Enya K, Kuramoto K, Sasaki S (2019) Science objectives of the Ganymede laser altimeter (gala) for the JUICE mission. Trans Jpn Soc Aeronaut Space Sci, Aerosp Technol Jpn 17(2):234–243. https://doi.org/10.2322/tastj.17.234

Kivelson MG, Khurana KK, Russell CT, Walker RJ, Warnecke J, Coroniti FV, Polanskey C, Southwood DJ, Schubert G (1996) Discovery of Ganymede's magnetic field by the Galileo spacecraft. Nature 384(6609):537–541. https://doi.org/10.1038/384537a0

Li C, Ren X, Liu J, Zou X, Mu L, Wang J, Shu R, Zou Y, Zhang H, Lü C, Liu J, Zuo W, Su Y, Wen W, Bian W, Wang M, Xu C, Kong D, Wang X, Wang F, Geng L, Zhang Z, Zheng L, Zhu X, Li J, Ouyang Z (2010) Laser altimetry data of Chang'E-1 and the global lunar DEM model. Sci China Earth Sci 53(11):1582–1593. https://doi.org/10.1007/s11430-010-4020-1

Luttrell K, Sandwell D (2006) Strength of the lithosphere of the Galilean satellites. Icarus 183(1):159–167. https://doi.org/10.1016/j.icarus.2006.01.015

Madden JH, Kaltenegger L (2018) A catalog of spectra, albedos, and colors of Solar System bodies for exoplanet comparison. Astrobiology 18(12):1559–1573. https://doi.org/10.1089/ast.2017.1763

Mizuno T, Kase T, Shiina T, Mita M, Namiki N, Senshu H, Yamada R, Noda H, Kunimori H, Hirata N, Terui F, Mimasu Y (2017) Development of the laser altimeter (LIDAR) for Hayabusa2. Space Sci Rev 208(1–4):33–47. https://doi.org/10.1007/s11214-015-0231-2

Moore WB, Schubert G (2000) The tidal response of Europa. Icarus 147(1):317–319

Moore WB, Schubert G (2003) The tidal response of Ganymede and Callisto with and without liquid water oceans. Icarus 166(1):223–226

Moore JM, Chapman CR, Bierhaus EB, Greeley R, Chuang FC, Klemaszewski J, Clark RN, Dalton JB, Hibbitts CA, Schenk PM, Spencer JR, Wagner RC (2004) In: Bagenal F, Dowling TE, McKinnon WB (eds) Jupiter. The planet, satellites and magnetosphere. Cambridge University Press, pp 397–426

Mukai T, Abe S, Hirata N, Nakamura R, Barnouin-Jha OS, Cheng AF, Mizuno T, Hiraoka K, Honda T, Demura H, Gaskell RW, Hashimoto T, Kubota T, Matsuoka M, Scheeres DJ, Yoshikawa M (2007) An overview of the LIDAR observations of asteroid 25143 Itokawa. Adv Space Res 40(2):187–192. https://doi.org/10.1016/j.asr.2007.04.075

Nimmo F, Pappalardo RT, Giese B (2002) Effective elastic thickness and heat flux estimates on Ganymede. Geophys Res Lett 29(7):1158. https://doi.org/10.1029/2001GL013976

Oberst J, Schreiner B, Giese B, Neukum G, Head JW, Pappalardo RT, Helfenstein P (1999) The distribution of bright and dark material on Ganymede in relationship to surface elevation and slopes. Icarus 140(2):283–293. https://doi.org/10.1006/icar.1999.6143

Palguta J, Anderson JD, Schubert G, Moore WB (2006) Mass anomalies on Ganymede. Icarus 180(2):428–441. https://doi.org/10.1016/j.icarus.2005.08.020

Palguta J, Schubert G, Zhang K, Anderson JD (2009) Constraints on the location, magnitude, and dimensions of Ganymede's mass anomalies. Icarus 201(2):615–625. https://doi.org/10.1016/j.icarus.2009.02.004

Palumbo P, Roatsch T, Lara LM, et al (2025) The JANUS (Jovis Amorum ac Natorum Undique Scrutator) VISNIR multi-band imager for the JUICE mission. Space Sci Rev 221

Pappalardo RT, Head JW, Collins GC, Kirk RL, Neukum G, Oberst J, Giese B, Greeley R, Chapman CR, Helfenstein P, Moore JM, McEwen A, Tufts BR, Senske DA, Breneman HH, Klaasen K (1998) Grooved terrain on Ganymede: first results from Galileo high-resolution imaging. Icarus 135(1):276–302. https://doi.org/10.1006/icar.1998.5966

Pappalardo RT, Belton MJS, Breneman HH, Carr MH, Chapman CR, Collins GC, Denk T, Fagents S, Geissler PE, Giese B, Greeley R, Greenberg R, Head JW, Helfenstein P, Hoppa G, Kadel SD, Klaasen KP, Klemaszewski JE, Magee K, McEwen AS, Moore JM, Moore WB, Neukum G, Phillips CB, Prockter LM, Schubert G, Senske DA, Sullivan RJ, Tufts BR, Turtle EP, Wagner R, Williams KK (1999) Does Europa have a subsurface ocean? Evaluation of the geological evidence. J Geophys Res, Planets 104(E10):24015–24055. https://doi.org/10.1029/1998je000628

Pappalardo RT, Collins GC, Head IJW, Helfenstein P, McCord TB, Moore JM, Prockter LM, Schenk PM, Spencer JR (2004) Geology of Ganymede. In: Bagenal F, Dowling TE, McKinnon WB (eds) Jupiter. The planet, satellites and magnetosphere. Cambridge University Press, pp 363–396

Pauer M, Musiol S, Breuer D (2010) Gravity signals on Europa from silicate shell density variations. J Geophys Res, Planets 115(E12):12005. https://doi.org/10.1029/2010JE003595

Prockter LM, Head JW, Pappalardo RT, Senske DA, Neukum G, Wagner R, Wolf U, Oberst JO, Giese B, Moore JM, Chapman CR, Helfenstein P, Greeley R, Breneman HH, Belton MJS (1998) Dark terrain on Ganymede: geological mapping and interpretation of Galileo regio at high resolution. Icarus 135(1):317–344. https://doi.org/10.1006/icar.1998.5981

Prockter LM, Lopes RMC, Giese B, Jaumann R, Lorenz RD, Pappalardo RT, Patterson GW, Thomas PC, Turtle EP, Wagner RJ (2010) Characteristics of icy surfaces. Space Sci Rev 153(1–4):63–111. https://doi.org/10.1007/s11214-010-9649-8

Rosenburg MA, Aharonson O, Head JW, Kreslavsky MA, Mazarico E, Neumann GA, Smith DE, Torrence MH, Zuber MT (2011) Global surface slopes and roughness of the moon from the lunar orbiter laser altimeter. J Geophys Res, Planets 116(E2):02001. https://doi.org/10.1029/2010JE003716

Schenk PM, Chapman CR, Zahnle K, Moore JM (2004) Ages and interiors: the cratering record of the Galilean satellites. In: Bagenal F, Dowling TE, McKinnon WB (eds) Jupiter. The planet, satellites and magnetosphere. Cambridge University Press, pp 427–456

Schmidt BE, Blankenship DD, Patterson GW, Schenk PM (2011) Active formation of 'chaos terrain' over shallow subsurface water on Europa. Nature 479(7374):502–505. https://doi.org/10.1038/nature10608

Schubert G, Zhang K, Kivelson MG, Anderson JD (1996) The magnetic field and internal structure of Ganymede. Nature 384(6609):544–545. https://doi.org/10.1038/384544a0

Schubert G, Anderson JD, Spohn T, McKinnon WB (2004) Interior composition, structure and dynamics of the Galilean satellites. In: Bagenal F, Dowling TE, McKinnon WB (eds) Jupiter: the planet, satellites and magnetosphere. Cambridge University Press, pp 281–306

Seabrook JA, Daly MG, Barnouin OS, Palmer EE, Gaskell RW, Nair H, Lauretta DS (2022) Building a high-resolution digital terrain model of Bennu from laser altimetry data. Planet Sci J 3(12):265. https://doi.org/10.3847/PSJ/aca011

Showman AP, Malhotra R (1997) Tidal evolution into the Laplace resonance and the resurfacing of Ganymede. Icarus 127(1):93–111

Sjogren WL, Wollenhaupt WR (1973) Lunar shape via the Apollo laser altimeter. Science 179(4070):275–278. https://doi.org/10.1126/science.179.4070.275

Smith DE, Zuber MT, Solomon SC, Phillips RJ, Head JW, Garvin JB, Banerdt WB, Muhleman DO, Pettengill GH, Neumann GA, Lemoine FG, Abshire JB, Aharonson O, Brown CD, Hauck SA, Ivanov AB, McGovern PJ, Zwally HJ, Duxbury TC (1999) The global topography of Mars and implications for surface evolution. Science 284:1495. https://doi.org/10.1126/science.284.5419.1495

Smith DE, Zuber MT, Phillips RJ, Solomon SC, Neumann GA, Lemoine FG, Peale SJ, Margot J-L, Torrence MH, Talpe MJ, Head JW, Hauck SA, Johnson CL, Perry ME, Barnouin OS, McNutt RL, Oberst J (2010) The equatorial shape and gravity field of Mercury from MESSENGER flybys 1 and 2. Icarus 209(1):88–100. https://doi.org/10.1016/j.icarus.2010.04.007

Smith DE, Zuber MT, Neumann GA, Mazarico E, Lemoine FG, Head JW III, Lucey PG, Aharonson O, Robinson MS, Sun X, Torrence MH, Barker MK, Oberst J, Duxbury TC, Mao D, Barnouin OS, Jha K, Rowlands DD, Goossens S, Baker D, Bauer S, Gläser P, Lemelin M, Rosenburg M, Sori MM, Whitten J, McClanahan T (2017) Summary of the results from the lunar orbiter laser altimeter after seven years in lunar orbit. Icarus 283:70–91. https://doi.org/10.1016/j.icarus.2016.06.006

Sohl F, Spohn T, Breuer D, Nagel K (2002) Implications from Galileo observations on the interior structure and chemistry of the Galilean satellites. Icarus 157(1):104–119

Spencer JR (1987) Thermal segregation of water ice on the Galilean satellites. Icarus 69(2):297–313. https://doi.org/10.1016/0019-1035(87)90107-2

Spohn T, Schubert G (2003) Oceans in the icy Galilean satellites of Jupiter? Icarus 161(2):456–467

Steinbrügge G, Stark A, Hussmann H, Sohl F, Oberst J (2015) Measuring tidal deformations by laser altimetry. A performance model for the Ganymede Laser Altimeter. Planet Space Sci 117:184–191

Steinbrügge G, Steinke T, Thor R, Stark A, Hussmann H (2019) Measuring Ganymede's librations with laser altimetry. Geosciences 9(7):320. https://doi.org/10.3390/geosciences9070320

Steinbrügge G, Voigt JRC, Wolfenbarger NS, Hamilton CW, Soderlund KM, Young DA, Blankenship DD, Vance SD, Schroeder DM (2020) Brine migration and impact-induced cryovolcanism on Europa. Geophys Res Lett 47(21). https://doi.org/10.1029/2020gl090797

Stephan K, Hibbitts CA, Jaumann R (2020) H2o-ice particle size variations across Ganymede's and Callisto's surface. Icarus 337:113440. https://doi.org/10.1016/j.icarus.2019.113440

Stephan K, Roatsch T, Tosi F, Matz KD, Kersten E, Wagner R, Molyneux P, Palumbo P, Poulet F, Hussmann H, Barabash S, Bruzzone L, Dougherty M, Gladstone R, Gurvits LI, Hartogh P, Iess L, Wahlund JE, Wurz P, Witasse O, Grasset O, Altobelli N, Carter J, Cavalié T, d'Aversa E, Della Corte V, Filacchione G, Galli A, Galluzzi V, Gwinner K, Hauber E, Jaumann R, Krohn K, Langevin Y, Lucchetti A, Migliorini A, Piccioni G, Solomonidou A, Stark A, Tobie G, Tubiana C, Vallat C, Van Hoolst T (2021) Regions of interest on Ganymede's and Callisto's surfaces as potential targets for esa's JUICE mission. Planet Space Sci 208:105324. https://doi.org/10.1016/j.pss.2021.105324

Thomas N, Hussmann H, Spohn T, Lara LM, Christensen U, Affolter M, Bandy T, Beck T, Chakraborty S, Geissbuehler U, Gerber M, Ghose K, Gouman J, HosseiniArani S, Kuske K, Peteut A, Piazza D, Rieder M, Servonet A, Althaus C, Behnke T, Gwinner K, Hüttig C, Kallenbach R, Lichopoj A, Lingenauber K, Lötzke H-G, Lüdicke F, Michaelis H, Oberst J, Schrödter R, Stark A, Steinbrügge G, del Togno S, Wickhusen K, Castro JM, Herranz M, Rodrigo J, Perplies H, Weigel T, Schulze-Walewski S, Blum S, Casciello A, Rugi-Grond E, Coppoolse W, Rech M, Weidlich K, Leikert T, Henkelmann R, Trefzger B, Metz B (2021) The BepiColombo laser altimeter. Space Sci Rev 217(1):25. https://doi.org/10.1007/s11214-021-00794-y

Tobie G, Choblet G, Sotin C (2003) Tidally heated convection: Constraints on Europa's ice shell thickness. J Geophys Res, Planets 108(E11). https://doi.org/10.1029/2003je002099

Tosi F, Roatsch T, Galli A, et al (2024) Characterization of the surfaces and near-surface atmospheres of Ganymede, Europa and Callisto by JUICE. Space Sci Rev 220:59. https://doi.org/10.1007/s11214-024-01089-8

Van Hoolst TG, Tobie G, Vallat C, et al (2024) Geophysical characterization of the interiors of Ganymede, Callisto and Europa by ESA's JUpiter ICy moons Explorer. Space Sci Rev 220:54. https://doi.org/10.1007/s11214-024-01085-y

Wahr JM, Zuber MT, Smith DE, Lunine JI (2006) Tides on Europa, and the thickness of Europa's icy shell. J Geophys Res, Planets 111(E12005):10

Witasse O, et al (2025) Space Sci Rev 221

Zharkov VN, Leontjev VV, Kozenko VA (1985) Models, figures, and gravitational moments of the Galilean satellites of Jupiter and icy satellites of Saturn. Icarus 61(1):92–100. https://doi.org/10.1016/0019-1035(85)90157-5

Zubarev A, Nadezhdina I, Oberst J, Hussmann H, Stark A (2015) New Ganymede control point network and global shape model. Planet Space Sci 117:246–249. https://doi.org/10.1016/j.pss.2015.06.022

Zuber MT, Smith DE, Lemoine FG, Neumann GA (1994) The shape and internal structure of the moon from the Clementine mission. Science 266(5192):1839–1843. https://doi.org/10.1126/science.266.5192.1839

Zuber MT, Smith DE, Cheng AF, Garvin JB, Aharonson O, Cole TD, Dunn PJ, Guo Y, Lemoine FG, Neumann GA, Rowlands DD, Torrence MH (2000) The Shape of 433 Eros from the NEAR-Shoemaker Laser Rangefinder. Science 289(5487):2097–2101. https://doi.org/10.1126/science.289.5487.2097

Authors and Affiliations

Hauke Hussmann[1] · Kay Lingenauber[1] · Alexander Stark[1] · Keigo Enya[2] · Nicolas Thomas[3] · Luisa M. Lara[4] · Christian Althaus[1] · Hiroshi Araki[5] · Thomas Behnke[1] · Jan Binger[1] · Doris Breuer[1] · Stefano Casotto[6] · Jose M. Castro[4] · Gaël Choblet[7] · Ulrich Christensen[8] · Willem Coppoolse[9] · Henri Eisenmenger[1] · Sylvio Ferraz-Mello[10] · Masayuki Fujii[11] · Naofumi Fujishiro[12] · Giovanni Gallina[9] · Klaus Gwinner[1] · Ernst Hauber[1] · Ulrich Heer[13,1] · Reiner Henkelmann[14] · Miguel Herranz[4] · Christian Hüttig[1] · Satoru Iwamura[15] · Jaime Jiménez[4] · Jun Kimura[16] · Okiharu Kirino[17] · Masanori Kobayashi[18] · Kei Kurita[19] · Valéry Lainey[20] ·

Thomas Leikert[14] · Alexander Lichopoj[1] · Horst-Georg Lötzke[1] · Fabian Lüdicke[1] · Ignacio Martínez-Navajas[4] · Harald Michaelis[1] · Hiroyuki Nakagawa[17] · Noriyuki Namiki[5] · Gaku Nishiyama[5,21,1] · Hirotomo Noda[5] · Jürgen Oberst[22] · Shoko Oshigami[23] · Antoine Pommerol[3] · Markus Rech[14] · Thomas Roatsch[1] · Rafael Rodrigo[4] · Adrián Rodríguez[24] · Kerstin Rösner[1] · Kazuyuki Touhara[2] · Yoshifumi Saito[2] · Sho Sasaki[16] · Yuki Sato[2,25] · Frédéric Schmidt[26] · Ulrich Schreiber[27] · Stefan Schulze-Walewski[9] · Frank Sohl[1] · Tilman Spohn[1] · Gregor Steinbrügge[28] · Katrin Stephan[1] · Kazuo Tanimoto[25] · Pascal Thabaut[1] · Simone del Togno[1] · Bert Vermeersen[29] · Henry Wegert[14] · Kai Weidlich[14] · Belinda Wendler[1] · Kai Wickhusen[1] · Mark Wieczorek[30] · Konrad Willner[1] · Friederike Wolff[1] · Takeshi Yokozawa[25] · Marie Yseboodt[31]

✉ H. Hussmann
hauke.hussmann@dlr.de

1 Institute of Planetary Research, German Aerospace Center (DLR), Berlin, Germany

2 Institute of Space and Astronautical Science, Japan Aerospace Exploration Agency, Sagamihara, Japan

3 Space Research and Planetary Sciences, Physics Institute, University of Bern, Bern, Switzerland

4 Instituto de Astrofisica de Andalucia, Granada, Spain

5 National Astronomical Observatory of Japan, Tokyo, Japan

6 University of Padua, Padua, Italy

7 University of Nantes, Nantes, France

8 Max Planck Institute for Solar System Research, Göttingen, Germany

9 Thales-Alenia Space Schweiz, Zürich, Switzerland

10 University of Sao Paulo, Sao Paulo, Brazil

11 FAM Science Co. Ltd., Tsukubamirai, Japan

12 Astro-Opt, Ichikawa, Japan

13 Airbus Defence and Space, Friedrichshafen, Germany

14 Hensoldt Optronics GmbH, Oberkochen, Germany

15 MRJ, Fujisawa, Japan

16 University of Osaka, Osaka, Japan

17 Crystal Optics Inc., Otsu, Japan

18 Planetary Exploration Research Center, Chiba Institute of Technology, Narashino, Japan

19 Earth-Life Science Institute, Institute of Science Tokyo, Tokyo, Japan

20 IMCCE, Paris, France

21 University of Tokyo, Tokyo, Japan

22 Technical University Berlin, Berlin, Germany

23 Terahertz Technology Research Center, National Institute of Information and Communications Technology, Tokyo, Japan

[24] Observatório do Valongo, Universidade Federal do Rio de Janeiro, Rio de Janeiro, Brazil

[25] MEISEI Electric Co. Ltd., Isesaki, Japan

[26] University of Paris-Saclay, Orsay, France

[27] Technical University Munich, Munich, Germany

[28] Jet Propulsion Laboratory, California Institute of Technology, Pasadena, United States of America

[29] Planetary Exploration, Technical University Delft, Delft, The Netherlands

[30] Institut de physique du globe de Paris, Université Paris Cité, CNRS, Paris, France

[31] Royal Observatory of Belgium, Brussels, Belgium